Journal of Materials Chemistry A

PAPER

Check for updates

Enhanced cycling stability of LiNiO$_2$ cathodes through a Mg/W dual-cation modification strategy

Beth I. J. Johnston, [ID] *[abc] Satish Bolloju,[ab] Stephen W. T. Price, [ID] [bd] Alexander G. Squires,[e] Lavan Ganeshkumar,[bf] Muhammad Ans,[ab] James A. Gott,[a] Narayan Simrit Kaur,[c] Innes McClelland, [ID] [bg] Samuel G. Booth, [ID] [bc] Andrew M. Beale,[d] Simon D. M. Jacques,[d] Ashok S. Menon, [ID] [ab] David O. Scanlon, [ID] [be] Louis F. J. Piper [ID] [ab] and Serena A. Cussen [ID] *[bg]

LiNiO$_2$ cathodes for lithium-ion batteries offer the prospect of high specific capacities; however, a plethora of structural and surface instabilities occur during cycling, which can limit their lifetime and impinge on their safety. Structural and surface modification strategies such as cation-doping have been shown to stabilise cycling performance and prolong cathode lifetimes, yet they often tackle either surface or bulk driven degradation processes. Here, we present a dual-cation substitution approach for the LiNiO$_2$ cathode which produces a coat-doped cathode in a single step. Judicious selection of cation substituents enables the targeted stabilisation of both bulk- and surface-originating instabilities, in this case magnesium and tungsten, respectively. While the addition of tungsten as a sole substituent promotes a rock-salt surface layer which typically reduces the observable capacity, we demonstrate that the incorporation of Mg into W-containing compositions can mitigate these structural transformations. These coat-doped Mg/W-LiNiO$_2$ cathodes exhibit superior cycling stabilities compared to unmodified LiNiO$_2$ and singly-substituted Mg- or W-LiNiO$_2$. X-ray diffraction computed tomography methods complement these findings, providing spatially resolved structural information on the location and heterogeneity of the coat-doped cathodes, guiding synthetic pathways to optimised materials that outperform undoped LiNiO$_2$ even in high-mass loading cell environments.

[a]WMG, University of Warwick, Coventry, CV4 7AL, UK. E-mail: beth.johnston@warwick.ac.uk
[b]The Faraday Institution, Quad One, Harwell Campus, Didcot, OX11 0RA, UK
[c]School of Chemical, Materials and Biological Engineering, The University of Sheffield, Sheffield, S1 3DJ, UK
[d]Finden Limited, Building R71, Rutherford Appleton Laboratory, Harwell, Oxford, OX11 0QX, UK

[e]School of Chemistry, The University of Birmingham, Birmingham, B15 2TT, UK
[f]Department of Chemistry, University College London, London, WC1H 0AJ, UK
[g]School of Chemistry, University College Dublin, Belfield, Dublin 4, Ireland. E-mail: serena.cussen@ucd.ie

Beth Johnston is an Assistant Professor at WMG, University of Warwick. She received her PhD from the University of Sheffield in 2021 under the supervision of Professor Serena Cussen developing microwave-based routes to cathode materials for lithium-ion batteries, followed by further postdoctoral research in the same group where she focused on developing stabilisation strategies to improve the cycle life of ultra-Ni-rich cathode materials. Currently, Beth's research centres on the synthesis and development of high-performance cathode materials, with a particular interest in scalable synthesis techniques and understanding the structure–property relationships that impact the material's functionality.

Beth I. J. Johnston

Introduction

The push towards global electrification of vehicle fleets to eliminate the damaging emissions from fossil-fuel powered vehicles has underpinned the demand for advances in Li-ion batteries and their component parts, particularly at the cathode.[1–3] Layered transition-metal oxide cathodes, of general formula $LiMO_2$, have carved out a prominent place in the commercial Li-ion battery market and the shift to higher nickel content chemistries such as NMCs ($LiNi_{1-x-y}Mn_xCo_yO_2$) and NCAs ($LiNi_{1-x-y}Co_xAl_yO_2$) has delivered significant improvements in energy densities.[4,5] This has concurrently reduced the cathode cobalt content, an element whose abundance is scarce and supply chain tenuous.[6] Eliminating cobalt completely represents a significant challenge, given its role in enabling high rate-capabilities and suppressing Li/Ni mixing, but it is possible,[7] with reports of high performing Co-free Ni-rich compositions such as $LiNi_{1-x-y}Mn_xAl_yO_2$ (NMAs) present in the literature.[8] In the case of cobalt-free $LiNiO_2$ (LNO), initial capacities in excess of 220 mA h g^{-1} at a voltage of 4.3 V $vs.$ Li/Li$^+$ are achievable.[9] In addition to eliminating cobalt, the removal of Mn can also be advantageous as this simplifies the synthetic route and increased specific capacity can be attained as the electrochemically inactive Mn^{4+} is no longer present.[10] Furthermore, LNO can serve as a model system for Ni-rich layered oxides, where an understanding of the fundamental behaviour of Ni in such compositions can be gained by deconvoluting the effects of multiple transition metals.[11] However, the high specific capacities of LNO are offset by poor capacity retention owing to various interlinked degradation pathways involving chemical, structural and thermal instabilities that can manifest as particle cracking, parasitic electrode–electrolyte reactions, transition metal (TM) dissolution, oxygen loss and surface reconstruction.[12,13] The sensitive surface chemistry of Ni-rich layered oxides further exacerbates these degradation processes, necessitating careful handling to avoid air exposure and ensure storage under inert environments to circumvent atmospheric aging which causes the formation of residual lithium species (e.g. Li_2CO_3) on the surface.[14–17] The surface sensitivity introduces further challenges at high states of charge where oxygen evolving from the surface may react with the electrolyte to further the formation of a cathode electrolyte interphase (CEI), transition metal dissolution and surface reconstruction to rock-salt type phases that increase charge transfer resistance.[18–20]

In addition to these complex surface degradation effects, bulk structural instabilities also occur and are principally linked to a lattice collapse that occurs at high states of charge for TM layered oxides.[21] These can be tracked through in situ and operando diffraction methods, which demonstrate several first-order phase transitions during cycling.[22–26] For LNO, during charging, these transitions proceed via H1 (pristine LNO) ↔ M ↔ H2 ↔ H3 where H denotes a hexagonal phase and M denotes a monoclinic phase. This is accompanied by a gradual decrease in the a lattice parameter throughout charging, motivated by the Ni–O environment which experiences oxidation during delithiation.

Meanwhile, the c lattice parameter gradually expands with lithium removal due to electrostatic repulsion between the $[NiO_2]$ layers until $\approx 80\%$ delithiation is reached. On reaching this point, which occurs between 4.15 V and 4.2 V $vs.$ Li/Li$^+$, the first order transition from the H2 to H3 phase is accompanied by a rapid c-axis contraction and lattice collapse, believed to be a result of the now almost empty Li layer where steric effects prevail over electrostatic repulsions.[27] The anisotropy between lattice parameter evolutions causes significant strain in the material.[28] Such induced strain in Ni-rich materials can manifest on the macroscale through particle cracking, which exposes fresh, highly reactive surfaces and can also lead to areas that become electronically disconnected.[29–31]

Attempts to mitigate such degradation modes and extend the cycling lifetime of LNO have previously included chemical stabilisation, such as surface coatings[32] or elemental substitution of Li or Ni with foreign cations. When small fractions of substituents are introduced (on the order of 0.5–5 mol%), we can consider this a substitution-type approach.[9,33,34] Substitution has proved to be an effective method in stabilising electrochemical performances in Ni-rich layered oxides with a wide variety of substituent cations able to stabilise cycling behaviour such as Al^{3+},[35–37] Mg^{2+},[38–40] Ti^{4+},[41–43] Ga^{3+},[44,45] B^{3+},[46,47] Zn^{4+}[48,49] and Nb^{5+}.[50] The location of the substituent can also influence the mode of stabilisation. For example Mg^{2+} is predicted to preferentially reside on Li$^+$ sites owing to the fact that it has a similar size to Li$^+$ ($r_{Li^+} = 0.76$ Å, $r_{Mg^{2+}} = 0.72$ Å) and a lower formation energy where it is thought to stabilise the $[LiO_2]$ interlayer against collapse through a pillaring effect.[51,52] More recently, high valence substituents which are more insoluble in the $LiMO_2$ structure, such as W^{6+}, Nb^{5+}, Ta^{5+}, and Mo^{6+}, have been investigated owing to their propensity to segregate to grain boundaries between particles where they may act to stabilise these surfaces during cycling.[53,54] Tungsten has also been shown to inhibit primary particle growth, in addition to suppressing the magnitude of the H2 ↔ H3 transition and improving the mechanical properties of LNO as a result of $Li_xW_yO_z$ surface phases which form.[55–58] Given different dopants can differently affect structure and stability, doping with multiple cations is an appealing prospect to access a combination of benefits for LNO cathodes.[59–61] Here, we consider the synergy between candidate substituent cations to deliver a coat-doped arrangement for LNO cathodes, combining the pillar-stabilising effects of magnesium within the particle bulk and the coating-stabilising effect of a tungsten-enriched surface phase. The efficacy of the dual-substitution strategy, utilising low substituent concentrations <2 mol% in total, was established through higher capacity retention, outperforming singly substituted LNO. While Mg-inclusion preserved the well-layered nature of the LNO structure, W incorporation was shown to promote a more rock-salt like structure and lower specific capacities. Through XRD-CT on charged samples, position-resolved crystallographic information revealed structural inhomogeneities across W-containing materials, prompting an improved synthetic strategy. Improved W-containing samples showed a more preserved layered oxide structure, leading to higher specific capacities. During cycling, the dual-substituted, coat-doped LNO consistently outperformed singly-substituted compositions across half- and full-cells, indicating promise in higher mass-

loading environments, demonstrating the efficacy of this targeted, scalable compositional tuning approach for high energy density ultra-Ni-rich cathode materials.

Experimental

Synthesis of doped and coat-doped LiNiO₂

A $Ni(OH)_2$ precursor was prepared *via* a precipitation method carried out in a stirred tank reactor (Eppendorf). Briefly, a 2 M $NiSO_4$ (from $NiSO_4 \cdot 6H_2O$, 99%, Thermo Fisher Scientific) solution was pumped into an NH_4OH solution (Merck) within the reactor. A 2 M NaOH (98%, Merck) solution (NaOH : TM ratio maintained at 2 : 1) and an NH_4OH chelating agent solution (NH_4OH : TM ratio = 5 : 1) were pumped separately into the reactor. The reaction was stirred overnight (1000 rpm) and a $Ni(OH)_2$ precipitate was obtained after washing. The powder was dried at 80 °C overnight.

The obtained $Ni(OH)_2$ powder was thoroughly mixed by grinding with $LiOH \cdot H_2O$ (99.995%, Thermo Fisher Scientific), WO_3 (99.9%, Merck) and $Mg(CH_3COO)_2$ (98%, Merck) in suitable quantities to obtain a total of six samples of target stoichiometries as follows: parent, unmodified $LiNiO_2$ (LNO), $Li_{0.99}Mg_{0.01}NiO_2$ (1Mg-LNO), $Li_{0.98}Mg_{0.02}NiO_2$ (2Mg-LNO), $LiNi_{0.99}W_{0.01}O_2$ (1W-LNO), $LiNi_{0.98}W_{0.02}O_2$ (2W-LNO) and $Li_{0.99}Mg_{0.01}Ni_{0.99}W_{0.01}O_2$ (1Mg1W-LNO). A molar excess of 1% $LiOH \cdot H_2O$ was used for synthesis initially, increasing to 5% for W-containing LNOs in later experiments (as described in the discussion). Ground samples were transferred to a tube furnace and heated at 480 °C for 5 hours followed by a final calcination at 770 °C (reduced to 710 °C for the parent LNO) for 15 hours under a flow of oxygen. After the reaction, samples were cooled to 200 °C and quickly removed to an Ar filled glovebox to avoid moisture and CO_2 uptake.

Materials characterization

Powder X-ray diffraction (PXRD) characterisation was carried out on a Rigaku Miniflex diffractometer using CuKα radiation operated at 40 kV and 15 mA. Data were collected in the 2θ range of 10 to 90° with a step size of 0.02°. Rietveld refinements were performed using the Generalized Structure Analysis System (GSAS-II).[62] The refinement process was carried out in the order (i) scale factor, (ii) 6 coefficient Chebyshev function background, (iii) sample displacement, (iii) cell parameters, (iv) crystallite size/strain parameters, and (v) site occupancies of Ni and Li in the Li layer, in which the total occupancy of Ni and Li was constrained to 1 for pristine LNO and W-LNO, or 0.99 for samples containing Mg. Although the Ni and Li occupancies were refined simultaneously according to the constraint, we do not infer the actual Li occupancy here due to the poor visibility of Li to X-rays. The isotropic atomic thermal displacement parameter (U_{iso}) was fixed.

Particle size and morphology were examined here using scanning electron microscopy (SEM). Samples were prepared on adhesive carbon tabs and coated with Au using a sputter coater to avoid charging feedback. SEM images were taken using an Inspect F50 electron microscope operating at 20 kV. Cross sectional electrode images (SEM and SEM-EDS) were acquired using a Thermo Fisher Scientific Scios Dualbeam system (operating at 2 kV and 0.1 nA), equipped with a CleanConnect inert gas transfer system. The method for ion milling and image acquisition is identical to that reported in previous work.[63]

Electrochemical measurements

Half-cells. For half-cell electrochemical tests, the LNO powders were mixed with C65 carbon black (Imerys) and poly-vinylidene fluoride (PVDF, Merck) in a weight ratio of 90 : 5 : 5 in NMP (*N*-methyl-2-pyrrolidone) solvent (Merck). The obtained slurry was cast onto carbon-coated Al foil using a doctor blade set at a height of 150 μm. The slurry was dried at 100 °C to evaporate the NMP solvent before further drying at 80 °C overnight in a vacuum oven. Electrodes of 10 mm diameter were then punched from the dried film and transferred into an Ar-filled glovebox. Active material loadings were 4–5 mg cm⁻².

CR2032 coin-type half-cells were constructed in an Ar-filled glovebox using the as-prepared LNO electrodes as the cathode, a 15.8 mm diameter Li metal anode (Cambridge Energy Solutions) and a Whatman glass microfibre separator. 100 μL of 1 M $LiPF_6$ in ethylene carbonate (EC) : ethyl methyl carbonate (EMC) (EC : EMC 3 : 7 by weight%) with 2% vinylene carbonate (VC) additive (Solvionic) was used as the electrolyte. Galvanostatic charge and discharge tests were carried out in a temperature-controlled chamber at 25 °C using an Arbin LBT21084 series cycler. In all cases 1C was defined as 220 mA g⁻¹. Initial slow cycles at C/10 or C/20 (as detailed in the text) were initially carried out using a constant-current constant-voltage (CCCV) protocol (current limits of C/20 and C/40 respectively), followed by longer term cycling at C/2 and/or C/3. Cells were cycled between 3.0 and 4.3 V *versus* Li/Li⁺ and 5 minute rest steps were implemented after each discharge. For *ex situ* XRD-CT tests, half-coin cells were cycled to defined upper cut-off potentials of 3.8, 4.2, 4.4 and 4.7 V *vs.* Li/Li⁺ at a rate of C/20. After reaching the desired cut-off voltage, cells were immediately disassembled in an argon filled glovebox, washed with dimethyl carbonate (DMC), dried under vacuum and stored under argon.

3 electrode full-cells

Electrode preparation. The cathode electrode was prepared by mixing either parent LNO or 1Mg1W-LNO, Super P, and PVDF (Solef 5130, Solvay) in a mass ratio of 90 : 5 : 5 (wt%) in NMP. The slurries were applied onto aluminium foil substrates using a precision drawdown coater (Erichsen Coatmaster 510). The active material loading was 13–14 mg cm⁻², and the electrodes were calendered to achieve a target density of 3.0 g cm⁻³. The anode electrode consisted of 95.25 wt% graphite (BTR V-H), 1 wt% carbon black (Imerys C45), 1.50% CMC (Ashland BVH8), and 2.25 wt% SBR (Zeon BM451) binder. The mass loading was 9.3 mg cm⁻², and the electrode was calendered to a density of 1.23 g cm⁻³. The negative to positive electrode capacity ratio (N/P) of electrodes was 1.17. The electrolyte used was 1 M lithium hexafluorophosphate ($LiPF_6$) in ethylene carbonate (EC) and ethyl methyl carbonate (EMC) (LP57) with 2% vinylene carbonate (VC) (Solvionic).

This journal is © The Royal Society of Chemistry 2025

J. Mater. Chem. A, 2025, **13**, 39077–39096 | **39079**

EL cell experimentation. The 3 electrode cell experiments were conducted using the PAT-EL-cell setup, with each cell containing 120 μL of electrolyte. Full cell charge–discharge testing was performed within a voltage window of 2.5 to 4.2 V *vs.* graphite on a BioLogic VMP3 potentiostat. Formation cycles were conducted at a constant current (CC) rate of C/20, while subsequent cycling was performed at a C/3 rate using a CC-constant voltage (CCCV) mode with a current cutoff at C/40, followed by CC discharge. Diagnostic cycles were carried out at C/20 after every 100 cycles. Electrochemical impedance spectroscopy (EIS) measurements were conducted on a BioLogic VMP potentiostat at 25 °C at 3.8 V (representing approximately 50% state of charge). Impedance was collected over a frequency range from 100 kHz to 10 mHz with a perturbation amplitude of 10 mV. After cycling, cells were disassembled and the cathode electrodes were harvested, washed with dimethyl carbonate solvent and subsequently dried and stored before analysis. All steps were conducted in an Ar filled glovebox.

X-ray diffraction computed tomography (XRD-CT)

XRD-CT measurements were performed on *ex situ* cathodes removed from cells at the denoted state of charge as described above. Washed and dried electrodes were cut into strips of *ca.* 10 × 3 mm. The narrow cross-section of the stacked samples helped avoid complications of parallax artefacts that can occur in XRD-CT measurements of large samples.[64] These strips were then stacked with layers with filter paper in between and set in resin. This stack of electrodes was affixed to a stub that was mounted atop the goniometer for measurements. The stack configuration was chosen to minimise the scan time needed for multiple planar samples and enabled direct comparison between electrodes within a single scan.

XRD-CT experiments were conducted at beamline P07 (EH2) of PETRA III, DESY. A monochromatic X-ray beam of 73.799 keV (0.168 Å) was focussed to 1 μm × 10 μm. Data was collected using a Pilatus3 X CdTe 2M detector and calibrated with a CeO₂ standard (99.9% <5 μm). XRD-CT scans were measured at 250 Hz with a translation step size of 1 μm, and 4 interlaced[65] rotational scans with steps of 0.72° within each scan, and steps of 0.18° between scans. The interlaced approach served firstly to assess for beam induced sample degradation, and secondly to mitigate the risk of unexpected failure during a very long duration scan.

XRD-CT processing and analysis

The raw 2D diffraction images were calibrated and azimuthally integrated using PyFAI,[66] to prepare sinograms consisting of translation × rotation × 1D powder diffraction patterns. During the data integration step, the data was processed both with and without a mean trimmed filter.[67] This filter is used to remove the artefacts that can occur from spotty single crystal diffraction (which would result in streak artefacts in the reconstructed images). It was noted that there was minimal difference in data quality between the filtered and non-filtered datasets, attributed to the beam size being much larger than the individual crystallite sizes within the sample. Therefore, the non-filtered data was used for the subsequent processing and analysis steps. Each separate scan had dimensions of 4000 × 501 pixels, and the final interlaced sinogram 4000 × 4001 pixels. A beam monitor diode was used in front of the beamstop to monitor the transmitted intensity through the sample. This value was used to correct the scattered intensity at each pixel to avoid absorption artefacts that could reduce the intensity of signals within the sample. The interlaced sinogram was reconstructed by filtered back projection using in-house Python scripts and then the data volume cropped tightly around the cathodes to reduce the overall size in memory to speed up analysis. The final voxel size in the reconstruction was 1 μm × 10 μm × 10 μm.

Phase identification of the reconstructed XRD-CT datasets was carried out using X'Pert HighScore Plus, whilst quantification of the datasets was carried out using BeamStop[68] (in-house high-volume data processing GUI) and Topas V7. For cathodes charged to higher voltages, two peaks corresponding to the $LiNiO_2$ (003) reflection with different *c*-axis lengths were observed in some pixels, *i.e.* there were regions smaller than the resolution of the measurement in the sample that had differing degrees of (de)lithiation in close proximity. To account for this in the refinement, two separate $R\bar{3}m$ $LiNiO_2$ models were used, with restrictions on the *c*-axis lattice parameter being above or below 14 Å. The analysis here focusses on probing the relative differences in the unit cell parameters per pixel, thus the $LiNiO_2$ models used here did not account for off-stoichiometry ($Li_{1-x}Ni_{1+x}O_2$ with *x* Ni^{2+} residing on the Li sites). Once fitting was completed, the scale factor for each $LiNiO_2$ phase was used to mask the respective lattice parameters and crystallite sizes, and then the results were combined to provide the average value per pixel presented in the figures below.

X-ray fluorescence computed tomography (XRF-CT)

XRF-CT experiments were performed at the ESRF using the Materials Science Beamline ID11. A monochromatic X-ray beam with an energy of 44 keV was focused using compound refractive lenses to have a spot size of *ca.* 150 × 150 nm² (horizontal × vertical), which also served as the translation step size, whilst the rotational step size was 0.249° over the range of 0–360°. The scans were measured using the continuous rotation scan method. The XRF patterns were acquired using a Sensicam CCD 2D fluorescence detector mounted vertically above the samples, with a dwell time of 10 ms per pixel. The XRF-CT data was also denoised[69] and reconstructed using the filtered back projection algorithm with in-house Python scripts.

Density functional theory

All Density Functional Theory (DFT) calculations were performed using the VASP plane-wave code with projector augmented wave (PAW) pseudopotentials.[70–73] Building upon our prior work on intrinsic defects in $LiNiO_2$,[74] calculations were expanded to include dopants W_{Ni}, W_{Mg}, W_i, Mg_{Ni}, Mg_{Li}, and Mg_i, and additional competing phases within the W–Li–Ni–O and Mg–Li–Ni–O phase spaces. The computational setup followed previous protocols: valence electrons considered

39080 | *J. Mater. Chem. A*, 2025, **13**, 39077–39096

This journal is © The Royal Society of Chemistry 2025

included Li $1s^2$ and $2s^1$, Ni 3d, O $2s^2$ and $2p^4$, Mg $3s^2$, and W $5s^2$ $5p^6$ $5d^6$ $6s^1$, using the HSE06 hybrid-DFT functional.[75,76] A plane-wave cutoff energy of 600 eV ensured energy convergence of 1 meV per atom, with a 30% higher cutoff (780 eV) for calculations that allowed volumes to relax to minimize Pulay stress.

Initial trial dopant-defect structures within Jahn–Teller distorted $LiNiO_2$ (space group $P2_1/c$) were generated using ShakeNBreak,[77,78] with low-energy configurations further optimized and analyzed with doped.[79] Defect relaxations used a $2 \times 4 \times 2$ supercell of the primitive $P2_1/c$ unit cell and were sampled with a $2 \times 2 \times 2$ Γ-centered Monkhorst–Pack k-point mesh. Convergence criteria were 1×10^{-5} eV for total energies and 0.01 eV Å^{-1} for forces.

Defect formation energies were calculated as:

$$\Delta E_x^f(q) = E_{tot}^x(q) - E_{tot}^{bulk} - \sum_i n_i(\mu_i + \Delta\mu_i) + q(E_F + E_{VBM}) + E_{corr}{}^q$$

where $E_{tot}^x(q)$ is the defect-containing supercell energy, E_{tot}^{bulk} is the defect-free reference energy, $\Delta\mu_i$ and μ_i represent changes and reference chemical potentials, respectively, E_F is the Fermi energy, E_{VBM} the host valence band maximum, and $E_{corr}{}^q$ the finite-size correction following Freysoldt et al.[80] Relevant chemical potentials were identified via CPLAP[81] based on thermodynamic stability limits. Defect concentrations were computed from the formation energies using py-sc-fermi (v3.0.0-beta)[82,83] accounting for site-exclusion effects.

Results and discussion

To examine the behaviour of Mg and W doping on $LiNiO_2$, a total of six compositions were prepared with an undoped LNO prepared as a baseline sample. Two samples containing 1 mol% of each substituent (denoted as 1Mg-LNO and 1W-LNO) were prepared to investigate the individual substituent effects on the LNO structure and performance and to establish whether any synergistic effect is observed upon dual coat-doping. As the coat-doped sample contains a total of 2 mol% substitution (denoted as 1Mg1W-LNO), additional samples containing 2 mol% of each individual substituent were also prepared (denoted as 2Mg-LNO and 2W-LNO) to deconvolute the effects of individual dopant species vs. dual coat-doping.

Materials characterization

Polycrystalline layered Ni-rich cathodes are typically comprised of micron-sized spherical secondary assemblies composed of tightly compacted, nanosized primary particles, so designed to improve tap densities in material application while minimising the surface area.[84] The morphology of the $Ni(OH)_2$ starting material is shown in Fig. S1, where spherical assemblies of typically 5 μm diameter are obtained through a carefully controlled precipitation reaction. Fig. 1(a) and (b) show the morphologies obtained for LNO and 1Mg1W-LNO (the morphologies obtained for all compositions LNO, 1Mg-LNO, 2Mg-LNO, 1W-LNO, 2W-LNO and 1Mg1W-LNO are shown in Fig. S2) where all materials at this stage were synthesised using

a 1 mol% $LiOH \cdot H_2O$ excess. The primary particles of W-containing samples are visibly smaller than those for pristine LNO and Mg-containing LNOs, highlighting the ability of the W substituent to restrict primary particle growth during calcination even at these low (1 mol%) levels, and may suggest some surface effect is at play where W-species accumulate at the primary particle grain boundaries. These microstructural changes caused by W-addition are likely attributed to two factors: (i) the lowering of the (003) facet surface energy, promoting rod-like particles and (ii) restriction of the primary particle coarsening from the segregation of W atoms to inter-particle boundaries, causing smaller primary particles.[85–87] Similar particle growth restriction has been reported for low-solubility substituents in Ni-rich layered oxides and could be beneficial as the smaller particles can more readily relieve the high strains associated with the H2 ↔ H3 transition.[53,54] For the Mg-containing LNOs here, there appears to be a slight increase in primary particle size between the parent LNO and Mg-containing LNO which is most likely associated with the higher calcination temperatures for these samples required to promote dopant incorporation into the structure, rather than an effect of the dopant. When calcined at these higher temperatures, the parent LNO indeed exhibits similar larger primary particle sizes (Fig. S3). In general, the quasi spherical-shape of the $Ni(OH)_2$ secondary particles is preserved after the calcination procedure (Fig. S4). SEM-EDS mapping of a 1Mg1W-LNO electrode (Fig. S5) shows the elemental distribution of Mg and W dopants throughout the secondary particles. A visually uniform distribution of both Mg and W is observed across the particles (Ni and O maps show clearly the location of the LNO particles), showing incorporation of the substituents at the secondary particle level. However, it is noted that an outlying bright region is clear in the W map outside of the particles, likely a piece of unreacted WO_3 precursor or a segregated section of Li_6WO_6 material.

To investigate the effect of both Mg and W substituents on the layered $LiNiO_2$ structure, samples were analysed by X-ray diffraction (XRD) and Rietveld refinement. Fig. 1(c) shows the powder XRD patterns obtained from LNO, 1Mg-LNO, 2Mg-LNO, 1W-LNO, 2W-LNO and 1Mg1W-LNO. The data have been normalised to the peak height of the (003) reflection for each sample. The observed diffraction peaks could be indexed to hexagonal type α-$NaFeO_2$ with space group $R\bar{3}m$ typical of transition metal layered oxide cathodes, with Li and Ni occupying alternating layers amongst a cubic close packed oxygen arrangement (Fig. S6). Fig. 1(d) magnifies the 2θ region where reflections from common impurity phases often appear between 20 and 35°. In this region, 1W-LNO and 2W-LNO show evidence of an impurity phase (marked with *) identified as Li_6WO_6.[56] These reflections in the 2W-LNO XRD pattern have a higher intensity indicating that the amount of Li_6WO_6 increases as the W substitution level increases. In contrast, compositions containing only Mg exhibit no evidence of Mg-containing impurities, suggesting Mg incorporation into the layered structure. For 1Mg1W-LNO, no Li_6WO_6 impurities are distinguishable from the background suggesting the ability of this dual cation strategy to mitigate the formation of the Li_6WO_6

This journal is © The Royal Society of Chemistry 2025

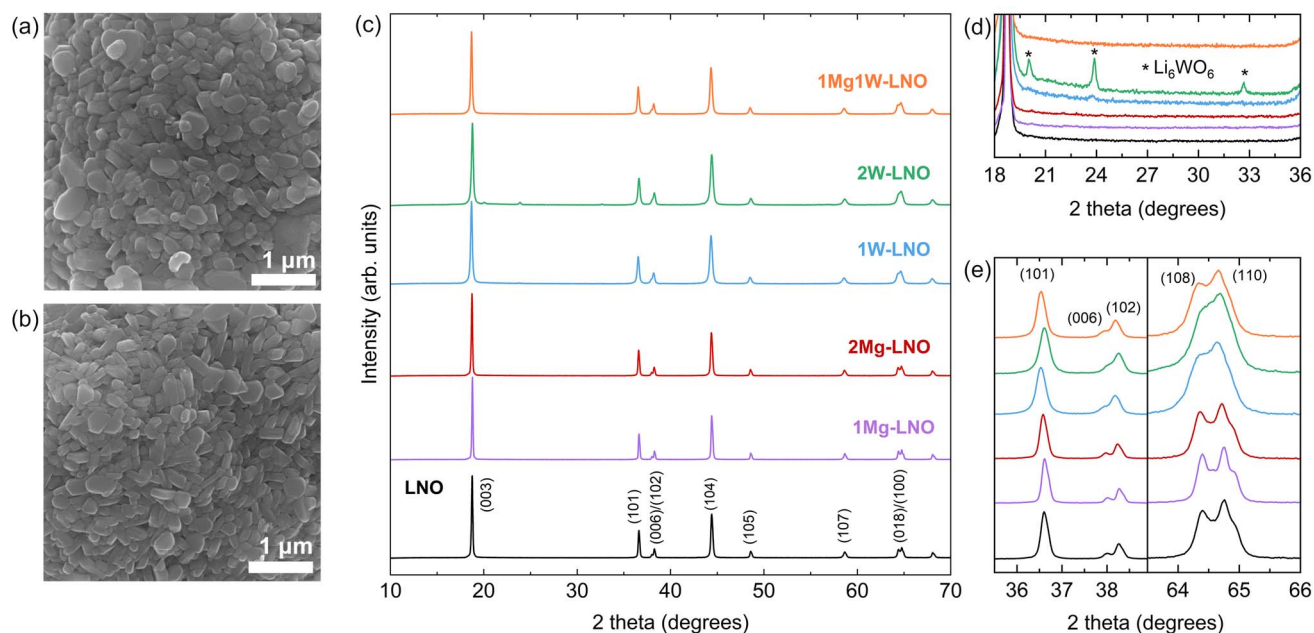J. Mater. Chem. A, 2025, 13, 39077–39096 | 39081

Fig. 1 Scanning electron microscopy images obtained for primary particles of (a) LNO and (b) 1Mg1W-LNO. (c) Powder X-ray diffraction patterns obtained for LNO, 1Mg-LNO, 2Mg-LNO, 1W-LNO, 2W-LNO and 1Mg1W-LNO highlighting the (d) 18 to 36° 2θ impurity region and (e) the (006)/(102) and (108)/(110) peak splitting.

phase. The mitigation of Li_6WO_6 formation during synthesis could be beneficial as such phases may leach lithium from $LiNiO_2$, leading to more rock-salt like, lithium deficient structures along the NiO–$LiNiO_2$ phase line, decreasing the practical capacities. For all samples here, no further impurities (*e.g.* Li_2CO_3, $LiOH$ and Li_2SO_4) are detected in the XRD data.

Fig. 1(e) highlights the (006)/(102) and the (108)/(110) peak doublets where the degree of splitting is an indication of the degree of layering in the crystal structure of $LiNiO_2$. These peaks coincide in the rock-salt structure, but as the structure begins to layer, they become increasingly separated.[9] Here, the degree of splitting appears reduced by W-substitution across 1W-LNO, 2W-LNO and 1Mg1W-LNO compared to pristine LNO and Mg-LNOs. This correlates well with the reported ability of W-substitution to reduce the layered character of the structure in favour of a more rock-salt like character[58,88] (although it is clear from the XRD data here that this structure remains predominantly layered in character). Vacancies in the Li layer likely promote a greater degree of off-stoichiometry in the samples and encourage a shift towards more rock-salt ($Li_xNi_{1-x}O$) behaviour, reducing the layering in the structure. However, upon coat-doping, improvements in peak splitting are seen here for 1Mg1W-LNO compared to 1W-LNO and 2W-LNO. As observed previously, the appearance of the Li_6WO_6 impurity for 1W-LNO and 2W-LNO, and its absence in 1Mg1W-LNO, suggest that the Mg-doping in W-LNOs can mitigate against the formation of Li–W–O species and help to preserve the Li content in the active layered phase and preserve more of its layered character.

To investigate the effect of Mg and W substitution on the $LiNiO_2$ structure in more detail, Rietveld refinements were performed as shown in Fig. 2(a) for LNO and (b) for 1Mg1W-LNO (Fig. S7(a) for 1Mg-LNO, (b) 2Mg-LNO, (c) 1W-LNO and (d) 2W-LNO) with structural parameters for all summarised in Table 1. Refinements undertaken assumed a hexagonal $NaFeO_2$ layered structure with space group $R\bar{3}m$ where Li occupies the 3a site, Ni occupies mainly the 3b site and oxygen occupies the 6c site. A Li_6WO_6 phase was added to the refinements for 2W-LNO where the associated peaks are clearly distinguishable from the background. A small amount of nickel was allowed to reside on the 3a site (denoted herein as Ni_{Li}) to represent the off-stoichiometry ($Li_{1-x}Ni_{1+x}O_2$) where the total occupancy of the 3a site was equal to unity. Li occupancy in the Ni layer was not considered as this is reported only to occur in LNO where the off-stoichiometry is high ($Ni_{Li} > 0.07$).[89] For Mg and W containing compositions, Mg was assumed to sit on the 3a site and W was assumed to fit in the 3b site and their occupancies were fixed at their theoretical value. Although W is predicted to accumulate at particle surfaces, a study by Bianchini *et al.* found that modelling the unit cell with W on 3b sites led to better quality fits.[58] Besides, at least some W incorporation into 3b sites is not completely ruled out and as a bulk averaged probe, XRD is unable to resolve the W distribution in the sample and from the XRD patterns exhibited in Fig. 1, it is clear here that the process of W-incorporation yields changes to the bulk LNO structure.

Compared to the undoped LNO, all doped samples display enlarged lattice parameters and thus enlarged unit cell volumes. Lattice parameter changes upon Mg and W-addition are compared in Fig. S8. Here, the laboratory X-ray measurements are not able to resolve the Mg positions for such a low doping level but its effect on the structural parameters can be
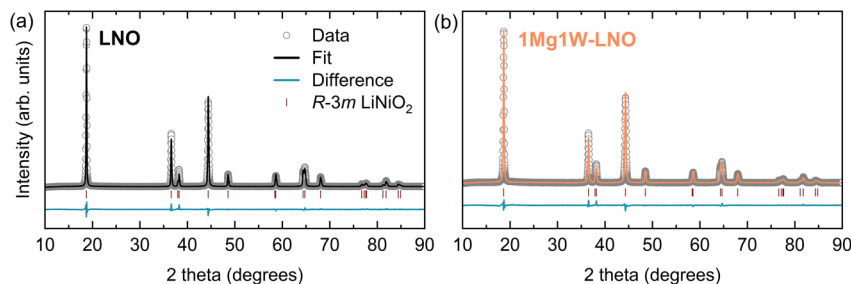
39082 | *J. Mater. Chem. A*, 2025, **13**, 39077–39096

This journal is © The Royal Society of Chemistry 2025

Fig. 2 Rietveld refinement plots of (a) LNO and (b) 1Mg-LNO showing the data (circles), fit (black/orange coloured line), difference (turquoise line) and the Bragg position ticks for $R\bar{3}m$ LiNiO$_2$ (red).

established. Upon addition of Mg^{2+} to LNO, the a-lattice parameter is found to expand at 1 mol% Mg but shrink for 2 mol% Mg while the c-lattice parameter grows for both 1 mol% and 2 mol% Mg, however not linearly. This behaviour is similar to that reported by Bianchini *et al.*[90] The reasons for such behaviour could lie in the distribution of Mg^{2+} over the 3a site (where it substitutes for Li) and the 3b site (where it substitutes for Ni). Here, laboratory X-ray measurements are not able to resolve the Mg positions and occupancies at low levels. For W-containing samples, both a- and c-lattice parameters and thus the unit cell volume increase in a linear fashion upon increasing W addition, consistent with previous reports and expected due to the larger ionic radius of W^{6+} compared to Ni^{3+}. For coat-doped 1Mg1W-LNO, only small changes compared to 1Mg-LNO and 1W-LNO occur. A small increase in the a-lattice parameter occurs from 1Mg-LNO to 1Mg1W-LNO accompanied by a minor increase in the c-lattice parameter, attributed to the reduction of Ni^{3+} in the Ni layer and additional Ni^{2+} in the interlayer as the off-stoichiometry increases. Meanwhile, no change in the a-lattice parameter is seen between 1W-LNO and 1Mg1W-LNO but the c-parameter is increased, likely a result of the interlayer spacing increasing on Mg-doping.

The c/a ratio, which is a commonly reported metric relating to the degree of layering in transition metal layered oxides such as LNO, is not greatly affected by Mg-substitution and slightly lowered on W substitution. This is seemingly increased for 1Mg1W-LNO, suggesting that the presence of Mg in W-containing compositions could aid in stabilising the layered phase over the rock-salt phase, also consistent with the trends observed in the (108)/(110) peak splitting behaviour observed in the XRD patterns (Fig. 1(e)). These trends are also reflected in the degrees of off-stoichiometry obtained, represented by the

amount of Ni^{2+} residing in the Li layer (Ni$_{Li}$) calculated from refinements. In general, as more Ni occupies the 3a sites the structure evolves from well-layered to one with more rock-salt like character. Minimal change is found between LNO, 1Mg-LNO and 2Mg-LNO where a small (<2%) fraction of Ni$_{Li}$ is calculated. A much larger degree of off-stoichiometry is found for 1W-LNO (4.5%) and 2W-LNO (6.2%), consistent with previous reports of W-doping into LNO.[57,58] For the coat-doped sample, 1Mg1W-LNO, the off-stoichiometry is decreased compared to 1W-LNO to 3.7%, further establishing the ability of dual-cation incorporation in reducing the extent of structural change affected by W-addition and helping to preserve more of the layered character of the LNO. While the total amount of non-Li atoms in the Li layer (Mg$_{Li}$ + Ni$_{Li}$) is consistent across 1Mg1W-LNO (assuming here total incorporation of Mg into the Li sites), 1W-LNO and 2W-LNO, reducing the amount of Ni$_{Li}$ defects is beneficial for mitigating against the possible local layer contractions reported from the reduction of Ni$_{Li}$ during charging (since the Mg oxidation state will stay constant).[51] So the benefits of dual substitution here are apparent in the suppression of unwanted Ni$_{Li}$ defects. While singly-doped LNOs have been shown here to behave in line with the literature, it should be noted that the benefits of coat-doping with Mg and W are shown to reverse, to some extent, the structural distortions brought about by W-addition and help to preserve the well-layered character of LiNiO$_2$, which will likely impact the electrochemical behaviour.

Dopant energetics

To support the structural characterisation of the cation substituted samples, we calculated the formation energies of relevant dopant-related defects under equilibrium conditions.

Table 1 Refined lattice parameters and degree of off-stoichiometry (Ni$_{Li}$) for LNO, 1Mg-LNO, 2Mg-LNO, 1W-LNO, 2W-LNO and 1Mg1W-LNO calculated from Rietveld refinements

Sample	a (Å)	c (Å)	V (Å^3)	c/a	Ni$_{Li}$	wR (%)
LNO	2.87741(4)	14.2039(3)	101.846(3)	4.936	0.016(1)	2.51
1Mg-LNO	2.87886(4)	14.2088(2)	101.983(3)	4.936	0.018(1)	2.53
2Mg-LNO	2.87837(4)	14.2094(3)	101.953(3)	4.937	0.014(1)	2.57
1W-LNO	2.87907(6)	14.2064(4)	101.981(5)	4.934	0.045(1)	2.16
2W-LNO	2.88076(7)	14.2096(5)	102.123(5)	4.933	0.062(1)	1.98
1Mg1W-LNO	2.87916(5)	14.2093(3)	102.009(4)	4.935	0.037(1)	1.96

Table 2 Chemical potential regimes at the vertices of the stability regions for Mg-doped LNO and W-doped LNO. The labels correspond to the labels given in Fig. 3

Mg-LNO	$\Delta\mu_{Li}$ (eV)	$\Delta\mu_{Ni}$ (eV)	$\Delta\mu_{O}$ (eV)	$\Delta\mu_{Mg}$ (eV)
A	−3.26	−2.93	0.00	−5.79
B	−3.04	−3.15	0.00	−5.73
C	−2.74	−2.85	−0.30	−5.43
D	−2.66	−2.60	−0.47	−5.28
E	−2.72	−2.39	−0.54	−5.25
F	−2.66	−2.45	−0.54	−5.23

W-LNO	$\Delta\mu_{Li}$ (eV)	$\Delta\mu_{Ni}$ (eV)	$\Delta\mu_{O}$ (eV)	$\Delta\mu_{W}$ (eV)
A	−3.26	−2.93	0.00	−9.79
B	−3.04	−3.15	0.00	−10.65
C	−2.74	−2.85	−0.30	−10.35
D	−2.66	−2.60	−0.47	−9.49
E	−2.72	−2.39	−0.54	−9.52
F	−2.66	−2.45	−0.54	−9.86

For Mg doping, the dopant species considered were Mg_{Ni}, Mg_{Li}, and Mg_i; for W doping, we included W_{Ni}, W_{Li}, and W_i. In both cases, defect concentrations were calculated at the vertices of the 4D chemical potential space that define the stability limits of Mg- and W-doped LNO. This approach allows us to investigate the bounds on the behaviour of the dopant species in LNO and how they interact with the intrinsic defect chemistry. The chemical potential stability limits for Mg and W doped LNO are given in Table 2.

For Mg-LNO, the predicted defect concentrations at these vertices and the interpolated paths between them are shown in Fig. 3(a). Two features of the plot stand out: firstly, the concentrations of the dopant defects are high relative to the intrinsic defect concentrations, suggesting that Mg incorporates into the bulk of LNO easily under most synthesis regimes, and secondly, that the preference for Mg substituting for Li and Ni is dependent on the chemical potentials of the cations which cannot be excluded as a potential contributor to the challenge of assigning the site preference of Mg dopants alongside instrument sensitivity. Repeating the same analysis for W-doped LNO (Fig. 3(b)) shows a stark difference from Mg-LNO. Here, there is a significant preference for W_{Ni} relative to W_{Li} in contrast to Mg-LNO where the preferred dopant site is dependent on the chemical potential limit the concentrations are calculated at, but also the concentrations of the W_{Ni} dopant species are significantly lower than most intrinsic defects. The concentrations are on the order of the nickel vacancy, which has been shown to be highly unstable in first principles studies.[91] From a thermodynamic perspective, bulk incorporation of W into layered LNO is unlikely. Any residual W content in the bulk of the material is likely to be due to out-of-equilibrium or kinetic effects; the system is likely to favour the segregation of W-rich phases. Thus, while the SEM-EDS mapping (Fig. S5) shows Mg and W distribution across the secondary particles, it is likely that while the Mg is doped into the bulk, W is segregated to the primary particle surfaces and grain boundaries (this scale is not resolvable in the EDS image).
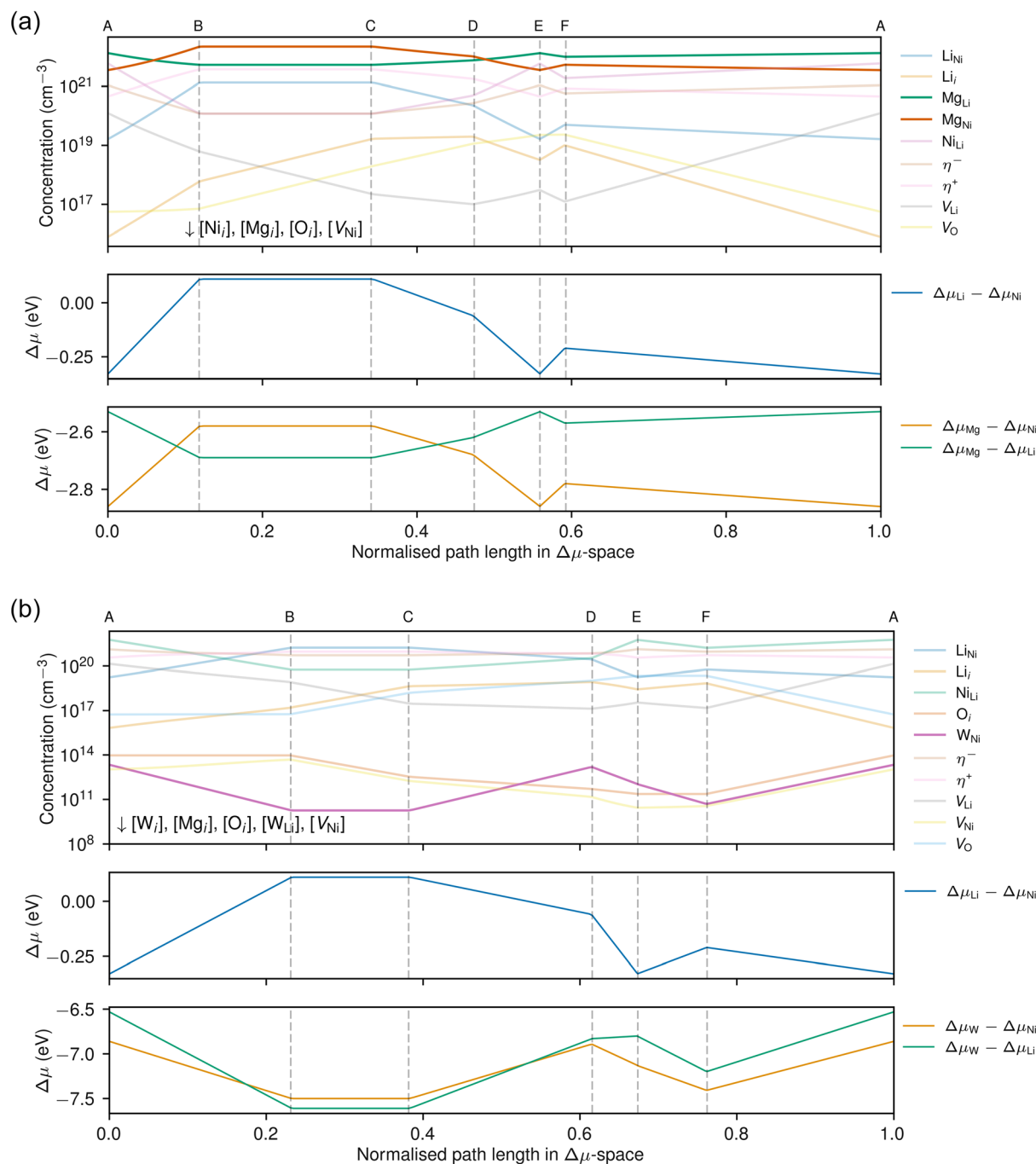
Electrochemical behaviour

Electrochemical tests were performed to evaluate the influence of Mg and W substitution on the cycling behaviour of LNO, most importantly to determine whether dual Mg/W-addition yields improved performance compared to singly doped compositions. Fig. S9 shows the first cycle charge and discharge profiles obtained for parent and cation substituted LNO compositions cycled in coin half-cells between 3.0 and 4.3 V vs. Li/Li$^+$ at a C/10 rate (where 1C = 220 mA g^{-1}) and at a constant temperature of 25 °C. Key parameters for the first cycle for all compositions are recorded in Table S1. Specific discharge capacities are lower for doped samples compared to undoped LNO as expected from the removal of active Li and/or Ni resulting from cation substitution. The capacity loss associated with W-containing samples is more severe than for those containing only Mg. For example, from LNO to 1Mg-LNO and 2Mg-LNO the discharge capacities fall from 216 to 208 and 206 mA h g^{-1}, respectively, indicating that there is only a small loss of capacity stemming from Mg-doping and negligible capacity loss upon increasing the Mg fraction from 1 mol% to 2 mol%. For W-containing samples, the discharge capacities fall to 194, 184 and 193 mA h g^{-1}, respectively, for 1W-LNO, 2W-LNO and 1Mg1W-LNO, demonstrating that an increasing molar fraction of 1 mol% to 2 mol% induces a further drop in capacity likely attributed to the increased off-stoichiometry and the higher detected amount of electrochemically inactive Li$_6$WO$_6$ phase. While the dual substituted 1Mg1W-LNO sample does not exhibit a further capacity decrease compared to 1W-LNO, there is no recovery in capacity as might be expected from the smaller off-stoichiometry compared to 1W-LNO. While the off-stoichiometry is relieved from 1W-LNO to 1Mg1W-LNO, the overall number of non-Li cations in the Li layer is overall unchanged when accounting for the Mg in the Li layer, which is likely to affect the discharge capacities in the same way.

On discharge, larger irreversible capacity losses are exhibited by all doped samples compared to the undoped LNO. Kinetic hindrances associated with greater off-stoichiometry are thought to govern first cycle losses in LNO.[92] So it is no surprise that all doped samples have higher irreversible capacities and poorer coulombic efficiencies compared to the undoped LNO material. However, if these capacity losses purely stem from local layer contractions around oxidised Ni$_{Li}$ at high states of charge,[93] this does not account for the larger irreversible capacities (compared to undoped LNO) observed in the Mg-doped LNOs. Instead, the revised mechanism for kinetic hindrances in off-stoichiometric LNO reported by Sicolo et al. explains the observed behaviour.[94] Here, positively charged Ni$_{Li}$ defects do not oxidise during charging but rather act as a sink for Li vacancies, preventing Li reintercalation to these vacancies under standard cycling conditions. For Mg-doped samples, the positively charged Mg$_{Li}$ should act in the same manner and induce Li vacancy (V$_{Li}$) trapping around it. Indeed, calculating Mg$_{Li}$–V$_{Li}$ binding energies as compared to Ni$_{Li}$–V$_{Li}$ binding energies, E_b, according tow

$$E_b = E^f_{M_{Li}, V_{Li}} - E^f_{V_{Li}} + E^f_{M_{Li}}$$

39084 | J. Mater. Chem. A, 2025, **13**, 39077–39096

This journal is © The Royal Society of Chemistry 2025

Fig. 3 Calculated defect concentrations across selected paths in the 4-dimensional chemical potential space for (a) Mg-doped and (b) W-doped LiNiO$_2$. (Top) Defect concentrations; (middle and bottom) cation chemical potential differences. The cation chemical potential differences are highlighted as the dominant intrinsic defects in doped LNO are intrinsic antisites and substitutional defects. Vertical dashed lines mark vertices defining stability boundaries explored in detail.

here M = Ni or Mg, the binding energy for the Mg$_{Li}$–V$_{Li}$ complex is found to be −0.92 eV as compared to −0.36 eV for Ni$_{Li}$–V$_{Li}$, suggesting that Mg^{2+} is a stronger trap for lithium vacancies than the Ni$_{Li}$ defect. The binding energies were found to be greatest when the lithium vacancy was in the next-nearest Li position as opposed to the vacancy being adjacent to the substitutional defect. The ability of any positively charged species in the Li layer to promote vacancy trapping and hinder relithiation explains well the irreversible capacity loss seen here across all doped compositions. Furthermore, from a geometric perspective, the immobile nature of these non-Li cations impedes Li diffusion by blocking potential migration pathways and lowering the kinetics of the system.[95]
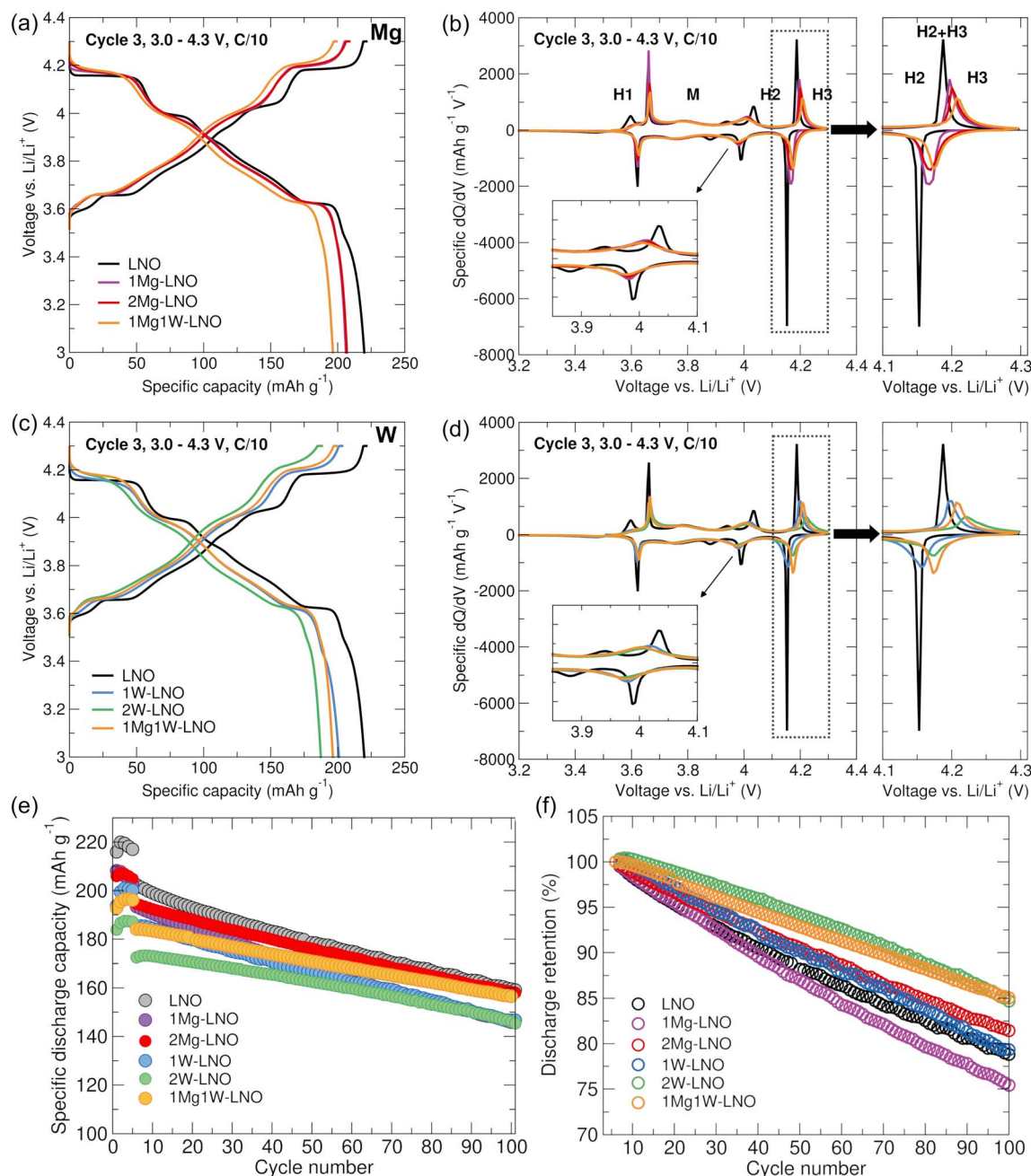
This journal is © The Royal Society of Chemistry 2025

J. Mater. Chem. A, 2025, **13**, 39077–39096 | **39085**

Fig. 4 Third cycle voltage profiles and differential capacity (dQ/dV) plots for (a and b) Mg-LNOs and (c and d) W-LNOs from galvanostatic cycling of half-coin cells between 3.0 and 4.3 V $vs.$ Li/Li$^+$ at C/10 at 25 °C. The (e) specific and (f) normalised (to the first cycle at C/2) capacity retentions of Mg- and W-LNOs. Cycling rates were set at C/10 for 5 cycles followed by C/2 (where 1C = 220 mA g^{-1}).

Fig. 4 shows the voltage-capacity profiles and the corresponding differential capacity (dQ/dV) plots for all LNO compositions during the third cycle. Fig. 4(a) and (b) show the effects on these for all Mg-containing samples while Fig. 4(c) and (d) highlight the changes observed for W-containing samples. Again, all substituted compositions exhibit lower discharge capacities compared to the undoped LNO. It should be noted that some compositions appear to have increased capacity compared to the first cycle, however this is commonly observed due to cathode conditioning processes that may occur.

The more sloping nature of the doped compositions (Fig. 4(a) and (c)) is clear. This is also reflected in the dQ/dV profiles in Fig. 4(b) and (d). Upon Mg and W incorporation, the peaks broaden, marking a shift from two-phase towards more solid-solution like behaviour. Suppressing the two-phase behaviour in favour of solid-solution behaviour is beneficial to the electrochemical performance and cycling stability as it can mitigate against pronounced volume changes at high states of charge which are known to induce particle cracking.[96] In particular, the feature at 3.9 V $vs.$ Li/Li$^+$ in the monoclinic region

39086 | J. Mater. Chem. A, 2025, 13, 39077–39096

This journal is © The Royal Society of Chemistry 2025

of the dQ/dV plots (magnified in each inset) corresponds to the stable ordering of Li vacancies in Li_xNiO_2 for $x = 2/5$ and is sensitive to structural modifications such as doping.[97] The Li vacancy orderings are disrupted by foreign cations (Ni_{Li} and Mg_{Li}) in the Li layer and thus this feature is suppressed in the substituted samples here. Similarly, the 3.5 V plateau on discharge, which is observed if the discharge (relithiation) kinetics are good, is also suppressed on substitution as a result of the foreign cations. The fact that this feature is suppressed even in Mg only containing samples (despite the similar Ni_{Li} amounts between LNO, 1Mg-LNO and 2Mg-LNO) is a strong indicator that Mg is present in the Li layer.

Further changes are clear in the H2 ↔ H3 transition that occurs between 4.1 and 4.2 V $vs.$ Li/Li$^+$ where the peaks broaden upon doping while also experiencing a shift to higher voltages. Broadening the H2 ↔ H3 peak can alleviate the severe and abrupt nature of the phase transition and help to mitigate the deleterious processes that originate from it, $e.g.$ the anisotropic lattice distortion leading to abrupt lattice collapse and particle cracking. It is clear from the magnification of the H2 ↔ H3 region in Fig. 4(b) and (d) that W-addition suppresses this phase transition to a greater extent than Mg-addition, although all doped samples show significant suppression of the H2 ↔ H3 peak compared to the undoped LNO. Fig. 4(b) highlights greater suppression for 1Mg1W-LNO than for 1Mg- and 2Mg-LNO, while 4(d) demonstrates increasing suppression on subsequent W-addition (LNO to 1W-LNO to 2W-LNO) while 1Mg1W-LNO is similar to 1W-LNO – suggesting that W-addition alters the H2 ↔ H3 transition characteristics more than Mg-addition (although both alter the behaviour compared to undoped LNO). The shift of the H2 ↔ H3 peaks to higher voltages on doping indicates a change in the thermodynamic potential of the transition during charge and discharge and is consistent with other reports of W and Mg containing LNOs.[57,58,90]

To assess the longer-term cycling behaviour of Mg and W containing LNOs, after 5 conditioning cycles at C/10, the current rate was increased to C/2. The specific capacities achieved across all compositions across 100 cycles are demonstrated in Fig. 4(e). Upon higher applied currents each composition experiences a capacity drop of approximately 10 to 15 mA h g^{-1} in line with kinetic expectations when moving to higher current values. After 100 cycles, undoped LNO, 2Mg-LNO and 1Mg1W-LNO all deliver specific capacities close to 160 mA h g^{-1}, while 1W-LNO and 2W-LNO exhibit lower capacities close to 150 mA h g^{-1}. However, by examining the normalised capacity retention (normalised to the specific discharge capacity achieved during the first cycle at C/2, Fig. 4(f)) the benefits of dual-substitution are clear. While pristine LNO retains approximately 77% of its initial capacity after 100 cycles, 1Mg1W-LNO displays superior retention of 85% after 100 cycles. Although the 2W-LNO sample achieved a similar normalised capacity retention to 1Mg1W-LNO here after 100 cycles, the disparity in specific capacity between these materials is evident. Overall, when considering both specific capacity and normalised capacity retention, the superior cycling behaviour of the 1Mg1W-LNO compared to the other compositions studied here

becomes evident and the implications of the Mg/W coat-doping strategy of LNO are promising.

However, despite the advantages of the dual-doped 1Mg1W-LNO shown here, the W-containing materials take a larger hit on capacity compared to the Mg only doped LNOs. The significant structural changes examined by PXRD (Fig. 1) and refinement of the XRD data (Fig. 2, S7 and Table 1), including the large calculated off-stoichiometries and the less layered character, likely lead to the reduction in capacity observed. The capacity drop observed on W-incorporation warrants improvements to the W-containing compositions. While the PXRD data presented here (above) yield information on the uncharged state of the LNOs, probing the structural evolution of the W-containing materials as a function of state of charge becomes important in determining suitable improvement strategies towards higher performance materials.

$Ex~situ$ XRD-CT analysis

Here we have employed the XRD-CT technique on the charged electrodes of LNO, 1W-LNO and 1Mg1W-LNO to spatially resolve these structural changes and examine how divergent the behaviour of W-containing LNOs becomes compared to the parent material under delithiation. XRD-CT is a combination of micro-focused XRD with computed tomography, with the final images being a cross section of the sample, where the contrast in the images arises from changes in the crystalline structure (rather than density contrast as in conventional X-ray absorption computed tomography). Each pixel in the reconstructed XRD-CT dataset has a unique XRD pattern containing crystallographic information, which can be refined in a similar manner to bulk powder XRD. Consequently, spatially resolved structural parameters (lattice parameters, crystallite size $etc.$) are obtained as a vertical cross-section through the cathode layer. This technique has been previously demonstrated in exploring the spatially resolved structural fatigue of Ni-rich $LiNi_{0.6}Co_{0.2}Mn_{0.2}O_2$ cathode materials where areas of high microstrain (identified as small particles and the surface of larger particles) were shown to undergo the well-known layered to spinel reconstruction.[98]

The XRD-CT measurements were performed on electrodes recovered from coin cells (see the Experimental), with each pixel in the image representing an area of roughly $10 \times 10~\mu m^2$ which is on the order of the secondary particle diameter. Thus, resolution on the secondary, but not primary particle level is expected. Only values extracted from the refinement of the $R\bar{3}m$ structure are shown, thus the Al current collector is not visible here. Each composition was charged up to an upper cut-off voltage between 3.8 V and 4.7 V $vs.$ Li/Li$^+$ at a slow C/20 rate to promote uniformity of Li removal through more kinetically favourable cycling conditions. The voltages chosen for analysis aim to provide a view of the cathode in the H1 phase (open circuit voltage, OCV) and the M phase (3.8 V), during the H2 → H3 transition (4.2 V), above the transition (4.4 V) and at extreme delithiation (4.7 V). Examining the evolution of the c lattice parameter in LNO at increasing states of charge allows for indirect monitoring of the homogeneity of the extent of
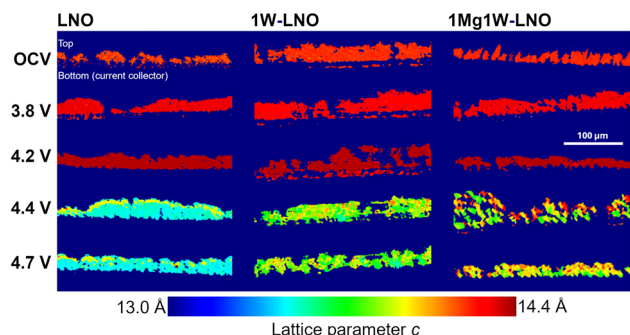
Fig. 5 Heat map of the *c*-lattice parameters obtained for LNO, 1W-LNO and 1Mg1W-LNO at OCV and charged up to 3.8 V, 4.2 V, 4.4 V and 4.7 V *vs.* Li/Li⁺ from Rietveld refinements of each pixel acquired through XRD-CT.

delithiation in the LNO compositions across the electrodes. This is shown in Fig. 5 for undoped LNO, 1W-LNO and 1Mg1W-LNO at the voltages stated above. All samples show a uniform expansion of the *c* lattice parameter across the area of examination up to 4.2 V, characterised by the deeper red colour observed at 4.2 V as compared to OCV and 3.8 V. This initial expansion in the *c* direction is well known owing to the stronger repulsion between adjacent oxygen slabs as lithium is initially removed from the layer.[9] Above 4.2 V the data show that all samples experience a *c*-axis contraction, visually represented through a shift to green/cyan. This occurs to a greater extent in undoped LNO compared to 1W-LNO and 1Mg1W-LNO, demonstrating the substituents' ability to suppress the phase transitions that induce structural instabilities (abrupt contraction of the *c*-axis during the H2 → H3 transition) that lead to interparticle cracking. Importantly however, the *c*-lattice parameter distribution is more spatially homogeneous in undoped LNO compared to the doped samples (seen also in the *a*-lattice parameter and the c/*a* ratio shown in Fig. S10(a) and (b)) which display a spread of colours across the electrode cross-section, representing a wider range of *c*-axis values within the sample. This is indicative of non-uniform delithiation characteristics across the doped cathodes. As the extent of delithiation ultimately determines the capacity, this non-uniformity could be the cause of the lower specific capacities observed across W-containing LNOs (1W-LNO, 2W-LNO, 1Mg1W-LNO). That some areas of the W-containing cathode powder respond differently under charging (deviating from the behaviour of the undoped LNO despite identical electrode and coin-cell fabrication protocols) suggests that inhomogeneity exists across the powder likely arising as a result of the synthetic protocol, advocating for a revised synthetic route. Inhomogeneity of W distribution is also observed in the particles, as examined on an OCV 1Mg1W-LNO electrode through X-ray fluorescence computed tomography (XRF-CT) shown in Fig. S11. It is also noted for undoped LNO charged up to 4.4 V (and persisting at 4.7 V), there exists a thin, distinct layer on the electrode surface of higher *c*-axis value (not observed in the *a*-axis values, Fig. S10(a)), indicative of a less oxidised, less delithiated surface[99] with a smaller degree of *c*-axis collapse.

W-containing LNOs synthesised with excess LiOH·H₂O

The inhomogeneity of the structural evolution during delithiation of W-containing LNOs compared to undoped LNO shown in the *ex situ* XRD-CT investigation suggests the need to tweak the synthesis of W-doped LNOs to improve their structural properties, ideally translating to improved electrochemical performances. To tackle the suggested lithium deficiency in the W-containing compositions, a higher LiOH·H₂O excess of 5 mol% was employed during synthesis (1 mol% was used previously). Previous work by Geng *et al.* has demonstrated that excess Li precursor added during synthesis for high W content (4 mol%) LNO could help in providing the lithium necessary to feed both $Li_xW_yO_z$ phases that accumulate at the grain boundaries and a well-layered bulk LNO phase.[56] Powder X-ray diffraction was carried out on this newly obtained sample set to determine if any changes in structure occurred upon this subtle change to the synthetic procedure. Owing to the success of the dual-substituted 1Mg1W-LNO shown prior, a 2Mg1W-LNO sample was also prepared here to probe whether further Mg-addition yielded further improvements. Fig. 6(a) shows the PXRD patterns collected for LNO, 1W-LNO, 2W-LNO, 1Mg1W-LNO and 2Mg1W-LNO where a 5 mol% LiOH·H₂O excess was used for each W-containing composition (the LNO displayed here is the same LNO as discussed previously, synthesised with 1 mol% LiOH·H₂O excess and is shown here to represent a baseline).

As before, the dominant peaks observed could be indexed to the $R\bar{3}m$ LNO structure. For all W-containing compositions the presence of Li_6WO_6 peaks is evident in the magnified impurity region ($19° \leq 2\theta \leq 35°$) where these peaks are higher in intensity for the 2W-LNO sample. In the previous 1Mg1W-LNO sample, no impurity peaks were observed, indicating that adding an excess of Li during the calcination can promote the formation of Li_xWO_y phases. It is likely that the formation of such lithium tungstates is favoured over W-incorporation into the layered structure. While all W-containing samples exhibit less peak splitting of the (108)/(110) compared to the baseline, the undoped LNO here (magnified in Fig. S12), no discernible differences in the (108)/(110) peak splitting are observed across the W-containing series, indicating that the layered structure formed is not vastly changed here as the dopant levels are changed and as dual cation substitution is exploited – in contrast to the changes that were observed in the previous samples.

To examine the structures in more detail, Rietveld refinements from the PXRD data were carried out in the same manner as discussed for the first sample set. The refinement plots for 1W-LNO and 1Mg1W-LNO are shown in Fig. 6(b) and (c), respectively, with the plots obtained from refinements of 2W-LNO and 2Mg1W-LNO being shown in Fig. S13 with structural parameters calculated from the refinements displayed in Table 3. The values for undoped LNO here are the same as those shown in Table 1 for the baseline LNO. As before, all doped samples possess larger unit cell parameters and volumes compared to the undoped LNO as expected for doped variants; however, this occurs to a lesser extent than for previously
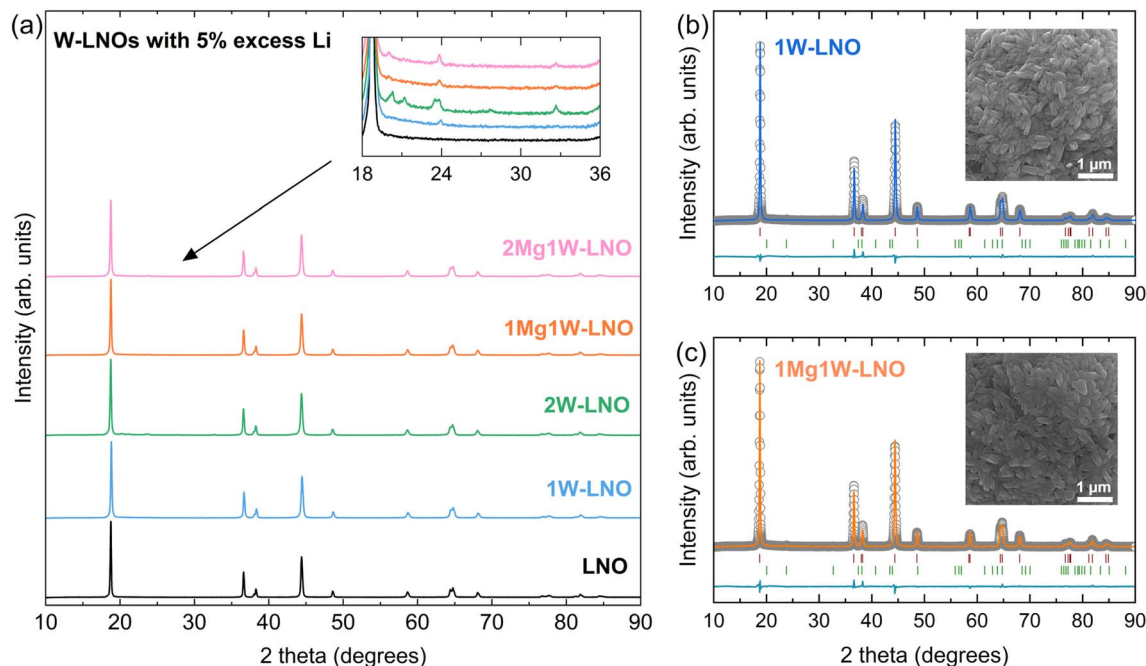
39088 | *J. Mater. Chem. A*, 2025, **13**, 39077–39096

This journal is © The Royal Society of Chemistry 2025

Fig. 6 (a) Powder X-ray diffraction patterns obtained for LNO, 1W–LNO, 2W–LNO, 1Mg1W–LNO and 2Mg1W–LNO with W-containing compositions synthesised with 5 mol% excess LiOH·H$_2$O. The inset highlights the 18 to 36° 2θ impurity region. (b and c) Rietveld refinement plots of 1W–LNO and 1Mg1W–LNO showing the data (circles), fit (blue/orange coloured line), difference (turquoise line) and the Bragg position ticks for $R\bar{3}m$ LiNiO$_2$ (red) and Li$_6$WO$_6$ (green). The insets show the primary particle morphologies obtained from SEM imaging.

Table 3 Refined lattice parameters and degree of off-stoichiometry (Ni$_{Li}$) for LNO, 1W–LNO, 2W–LNO, 1Mg1W–LNO and 2Mg1W–LNO (with W-containing compositions synthesised with 5 mol% excess LiOH·H$_2$O) calculated from Rietveld refinements

Sample	a (Å)	c (Å)	V (Å^3)	c/a	Ni$_{Li}$	wR (%)
LNO	2.87741(4)	14.2039(3)	101.846(3)	4.936	0.016(1)	2.51
1W–LNO	2.87835(5)	14.2052(3)	101.922(4)	4.935	0.028(1)	2.14
2W–LNO	2.87947(4)	14.2098(1)	102.033(3)	4.935	0.028(1)	2.15
1Mg1W–LNO	2.87814(5)	14.2046(3)	101.902(4)	4.935	0.020(1)	2.15
2Mg1W–LNO	2.87847(5)	14.2095(3)	101.960(4)	4.936	0.014 (1)	2.17

observed doped samples (Table 1), indicating less deviation away from the structural properties of undoped LNO when using a greater Li precursor excess during synthesis. This behaviour could indicate a more well-layered structure attained through relieving the Li deficiency that can occur on formation of Li$_x$W$_y$O$_z$ phases. The structural changes brought about by this extra Li during synthesis are perhaps most clear through the Ni$_{Li}$ values obtained from the refinements. While an increase in Ni$_{Li}$ is observed for the 1W–LNO here at 2.8% this is much lower than the previous value of 4.5% obtained for 1W–LNO in the previous sample set and it is likely that the additional Li helps to mitigate against Ni migration into the Li layer. This is similarly observed for the 2W–LNO sample here compared to the previous 2W–LNO sample (1 mol% excess LiOH·H$_2$O during synthesis); however, here, there is no increase in the Ni$_{Li}$ value on doubling the W-content from 1W–LNO to 2W–LNO despite increasing lattice parameters. The slightly enlarged c-parameter in the absence of additional Ni$_{Li}$ defects could be caused by a slight Li deficiency in the Li layer

that does not promote further off-stoichiometry. The structural changes could originate from the removal of Li from the layered structure to accommodate the Li$_6$WO$_6$ phase – so, a more Li deficient layered phase for 2W–LNO compared to 1W–LNO which does not cause a detectable change in the off-stoichiometry. Consistent with the results demonstrated for the previous Mg/W-doped sample set, the coat-doping is shown to reduce the off-stoichiometry from 2.8% to 2.0%, further confirming the ability of the Mg-dopant to mitigate against Ni migration in high-valence doped LNO compositions. Doubling the Mg-content in the coat-doped samples further demonstrates this, where for 2Mg1W–LNO the Ni$_{Li}$ quantity was calculated to be 1.4% from the refinement, which brings this value in line with that calculated for undoped LNO (although the total amount of non-Li atoms in the Li layer will be larger after accounting for Mg$_{Li}$).

Electrochemical tests were conducted to examine two outcomes: (i) whether the improved structural properties of W-containing LNOs translated to improved electrochemical
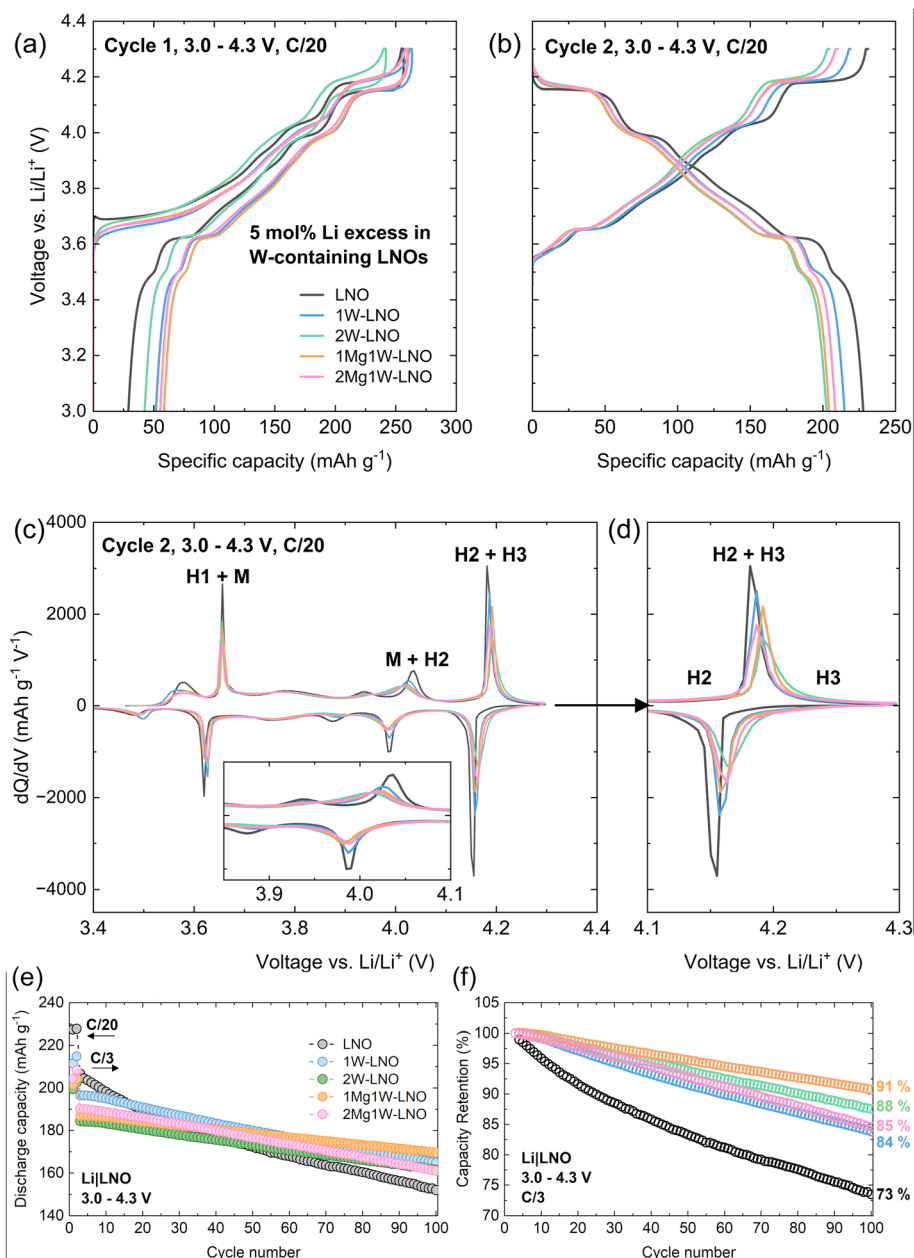
This journal is © The Royal Society of Chemistry 2025

J. Mater. Chem. A, 2025, **13**, 39077–39096 | **39089**

Fig. 7 (a) First and (b) second cycle charge–discharge profiles, (c) second cycle differential capacity (dQ/dV) plots, (d) expanded view of the 4.1 to 4.3 V $vs.$ Li/Li$^+$ dQ/dV region encompassing the H2 to H3 transition and comparison of (e) specific discharge capacity stability and (f) normalised discharge capacity retention for LNO, 1W-LNO, 2W-LNO, 1Mg1W-LNO and 2Mg1W-LNO from galvanostatic cycling of half-coin cells between 3.0 and 4.3 V $vs.$ Li/Li$^+$ at 25 °C.

properties and (ii) to examine whether the enhanced stability imparted through Mg/W coat-doping was consistent across both sample sets. A clear increase in initial capacity for 1W-LNO is afforded when a greater LiOH·H$_2$O excess is employed during the synthesis shown in Fig. S14, demonstrating the advantage of this in W-containing LNOs. Fig. 7(a) shows the first cycle voltage-capacity profiles for LNO, 1W-LNO, 2W-LNO, 1Mg1W-LNO and 2Mg1W-LNO cycled between 3.0 and 4.3 V at a current rate of C/20 (where 1C = 220 mA g^{-1}) at 25 °C, with Table S2 summarising the first cycle characteristics. Upon charging, LNO and doped compositions containing 1 mol% W

reach similar capacities in the region of ~260 mA h g^{-1}; however, that of 2W-LNO is reduced to ~240 mA h g^{-1}. Although the quantity of Ni$_{Li}$ defects in 1W-LNO and 2W-LNO was calculated to be the same, we cannot infer the Li content in the samples from the Ni$_{Li}$ concentration due to the poor visibility of Li to X-rays which renders refinements of Li contents non-sensical. While they share a common off-stoichiometry, there is a clear enlargement of the unit cell parameters and cell volume for 2W-LNO compared to 1W-LNO (Table 3), suggestive of a Li deficiency in 2W-LNO. A combination of excess Li$_x$W$_y$O$_z$ phases and a Li deficiency in 2W-LNO is likely to

account for the reduced capacity for 2W-LNO. Interestingly, however, Hua *et al.* explored how surface Li$^+$ vacancies could improve the electrochemical properties in Li-rich layered oxide cathode materials, where creating a shell with Li$^+$ vacancies was shown to drastically improve the first cycle coulombic efficiencies and the resulting cycle life through improving the bulk phase activity and redox kinetics.[100] Here, while suggested Li$^+$ deficiencies can lower the specific capacities of LNO, the effect on capacity stabilisation is clear. On discharge, poorer first cycle coulombic efficiencies/larger irreversible capacity losses are exhibited by all doped samples compared to the undoped LNO as observed in the first sample set. However, for all samples here, the discharge plateau at 3.5 V, indicative of good lithiation kinetics, is not suppressed in any W-containing samples, likely due to the improved off-stoichiometries afforded by the altered synthesis route.

Fig. 7(b) shows the voltage profiles during the 2nd cycle in coin half-cells where all materials now exhibit discharge capacities >200 mA h g^{-1} with the trend LNO > 1W-LNO > 2Mg1W-LNO > 2W-LNO ≈ 1Mg1W-LNO. The capacity penalty associated with the first cycle irreversible capacity loss determines this trend with the doped materials all displaying lower capacities compared to the undoped LNO as observed before. Higher initial specific capacities are obtained when doubling the Mg content from 1 mol% to 2 mol% here between 1Mg1W-LNO and 2Mg1W-LNO and higher overall specific capacities are achieved when increasing the LiOH·H$_2$O excess during synthesis from 1 mol% to 5 mol% for W-containing LNOs attributed to the decrease in off-stoichiometry in the samples.
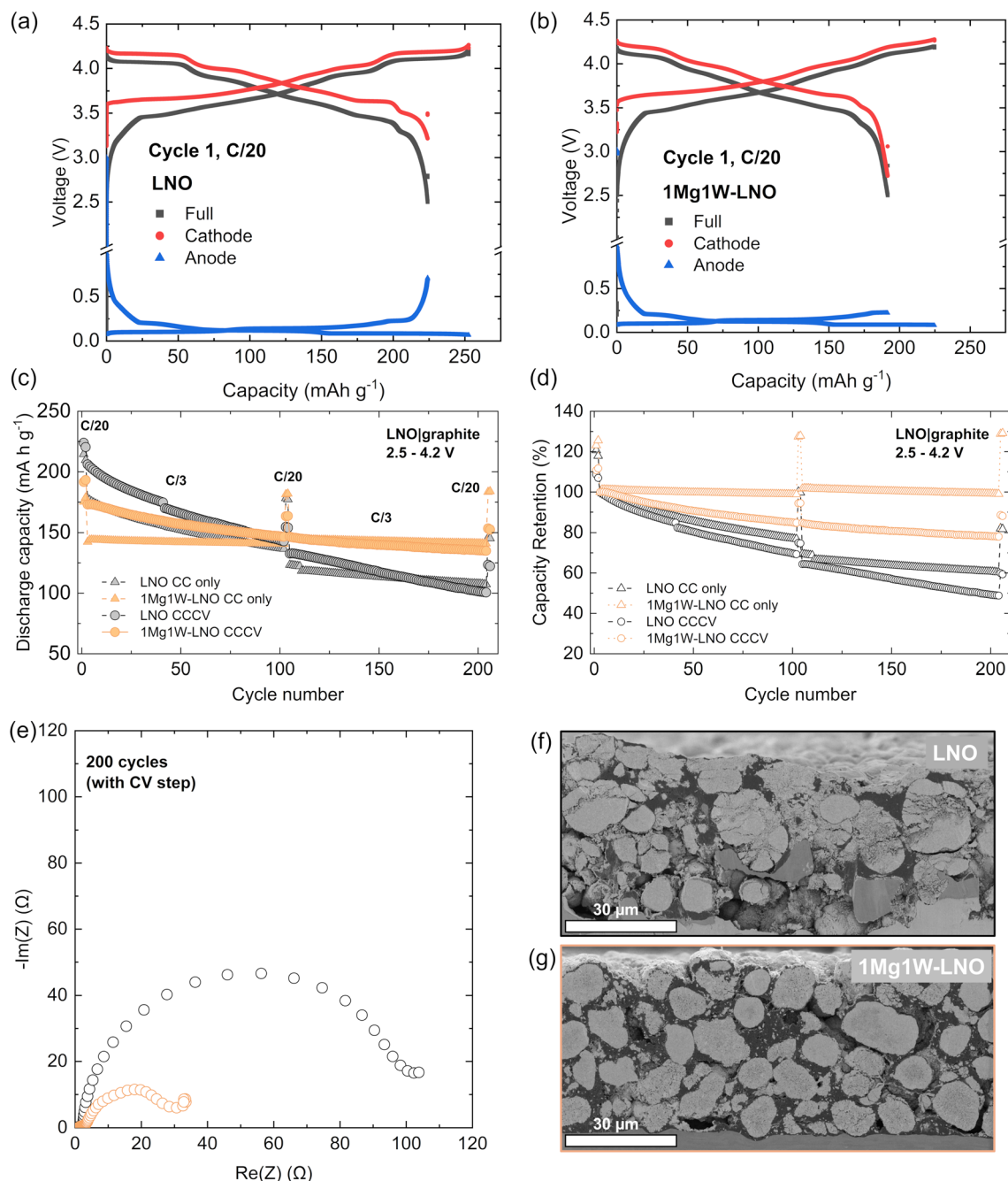
The differential capacity (dQ/dV) profiles for the 2nd cycle are shown in Fig. 7(c) where the LNO phase transitions during de/lithiation are observed for all samples. As before, on dopant incorporation, the peaks become less intense and broader as the phase transition behaviour becomes more solid-solution like. The minimum at ~3.9 V *vs.* Li/Li$^+$ associated with the stable lithium/vacancy ordering at x = 2/5 (in Li$_x$NiO$_2$) also disappears here for all doped materials, mirroring the behaviour displayed for the doped LNO samples discussed above. The H2 ↔ H3 transition (Fig. 7(d)) also mirrors the previous samples' behaviour where the peak associated with the transition becomes broader, in agreement with expectations. Within this sample set, the suppression in both coat-doped samples (1Mg1W-LNO and 2Mg1W-LNO) lies between that of 1W-LNO and 2W-LNO, indicating that in these compositions W addition has more of a suppressive effect on the transition than Mg. While suppression generally leads to more stable cycling in these materials and is seen as a favourable outcome, it is often at the expense of capacity and a middle-ground must be sought. To assess the longer-term cycling behaviour of these doped LNOs, after two formation cycles at C/20, the current rate was increased to C/3 and the performance was assessed over 100 cycles. The specific capacities of LNO, 1W-LNO, 2W-LNO, 1Mg1W-LNO and 2Mg1W-LNO are shown in Fig. 7(e) with the normalised capacity retention in 7(f). Upon increase of current density, the capacity for each composition drops between 10 and 15 mA h g^{-1}. After 100 cycles, the capacity delivered by the dual-doped 1Mg1W-LNO (170 mA h g^{-1}) is higher than that of

undoped LNO (152 mA h g^{-1}) and the other doped compositions (165 and 161 mA h g^{-1} for 1W-LNO and 2W-LNO, respectively). When normalised, the enhancement provided to the capacity retention by the coat-doping is even more clear. After 100 cycles, 1Mg1W-LNO retained 91% of its starting capacity (at C/3) compared to 74% for undoped LNO and 84 and 88% for 1W-LNO and 2W-LNO, respectively. As before (under initial synthesis conditions employing 1 mol% of LiOH·H$_2$O precursor), the coat-doped sample 1Mg1W-LNO exhibits improved cycling stability.

Three-electrode cell performance

The cell performance of LNO and 1Mg1W-LNO was further assessed in 3-electrode (3E) cells with LNO, graphite and lithium metal as the active, counter and reference electrodes, respectively. The 3E format (Fig. S15) allows tracking of the individual cathode and anode electrochemical behaviour during cycling. Use of a graphite anode in this set-up also allows the system to operate as a full cell compared to the half-cell behaviour shown earlier. Full cells further allow the cycling performance to be evaluated under more realistic conditions, *e.g.* without the large excess of lithium provided by thick metallic anodes and at higher cathode mass loading levels closer to those used in larger cell formats. Here, we employ a mass loading roughly 3 times greater than for half-cells (see the Experimental). The voltage-capacity data for LNO and 1Mg1W-LNO during the first and second cycles at C/20 is shown in Fig. 8(a) and (b). Similar to the half-cell data, undoped LNO delivers higher initial specific capacity (~225 mA h g^{-1}) as compared to 1Mg1W-LNO (~200 mA h g^{-1}). While there is no improvement in the first cycle coulombic efficiency for LNO between half- (Table S2) and full-cell configurations where ≈ 88% CE is observed, there is an improvement seen for 1Mg1W-LNO from approximately 78% to 85%. One key difference in electrode production here is also the use of calendering in the higher mass loading electrodes. Calendering likely improves the electrode kinetics of the doped system at C/20 as compared to the uncalendered electrode, where kinetic hindrances have been demonstrated to induce larger first cycle capacity loss as previously described.[92] Already sufficient kinetics in the undoped LNO likely preclude an observable difference for this composition. The long-term cycling performance was also evaluated in this cell format, with the specific and normalised capacity retentions over 200 cycles shown in Fig. 8(c) and (d). For the cycling tests here, two conditions were tested at the top of charge: constant current (CC) charging with and without a constant voltage (CV) step. When implementing a CC-only charging protocol, both LNO and 1Mg1W-LNO display lowered discharge capacities at C/3. While 1Mg1W-LNO (CC only) here displays lower capacities of ~145 mA h g^{-1}, it is extremely stable across 200 cycles with close to 100% capacity retention, while LNO retains only 60% of its initial C/3 capacity. Application of a CV step at the top of charge was shown to promote higher capacities and aggravated capacity fade across both samples as compared to cells with no CV step. This interplay between capacity and stability invokes

This journal is © The Royal Society of Chemistry 2025

J. Mater. Chem. A, 2025, **13**, 39077–39096 | **39091**

Fig. 8 First cycle voltage-capacity profiles obtained for (a) undoped LNO and (b) 1Mg1W-LNO from 3E cells, showing the individual cathode and anode behaviour and that of the full-cell. The (c) specific and (d) normalised capacity retention of both materials in 3E cells over 200 cycles at C/3 utilising both CC only and CCCV charging protocols. (e) Nyquist plots of the cathode component EIS data collected from 3E cells at 3.8 V for undoped LNO and 1Mg1W-LNO after 200 cycles at C/3 (using a CCCV charging protocol). Post cycling cross sectional SEM images of (f) LNO and (g) 1Mg1W-LNO electrodes harvested after 200 cycles from EL-CELLs using the CC only charging protocol.

the critical issue with layered oxide materials, where greater extents of delithiation (enabled through the CV step here) aggravate physicochemical phenomena leading to material degradation and performance fade.[21] However, after 200 cycles, it can be clearly seen that 1Mg1W-LNO outperforms undoped LNO in terms of both specific and normalised capacity retention, under both charging protocols implemented here. Furthermore, while LNO (CC only) and 1Mg1W-LNO (CCCV)

initially deliver similar C/3 capacities between ~173 and 178 mA h g^{-1}, the coat-doped sample displays significantly more stable performance after 200 cycles, indicative of the stabilising role that the dopants play in these systems with similar starting capacities. The diagnostic cycles, performed every 100 cycles, also demonstrate the ability to recover a significantly higher proportion of the C/20 capacity in the

39092 | J. Mater. Chem. A, 2025, 13, 39077–39096

This journal is © The Royal Society of Chemistry 2025

1Mg1W-LNO samples and may reflect lower Li inventory loss for the doped systems.

For the 3E cells cycled with a CCCV charging protocol above, electrochemical impedance spectroscopy (EIS) was performed to evaluate the evolution of the cell impedances over long term cycling across parent LNO and coat-doped 1Mg1W-LNO, yielding insights into surface degradation. The Nyquist plots generated using 200 cycles of EIS data obtained from the cathode component of the 3E cell for LNO and 1Mg1W-LNO are shown in Fig. 8(e). The Nyquist plots generated using the full EIS data (cathode, anode and full cell) after formation, after 100 cycles and after 200 cycles are shown in Fig. S16, where the majority of the cell impedance contribution comes from the cathode during aging. After formation (Fig. S16(a) and (d)), a lower frequency semicircle attributed to the charge transfer resistance dominates, followed by a Warburg type impedance tail. Here, the 1Mg1W-LNO cathode exhibits an initial higher charge-transfer resistance compared to the parent LNO, likely from the hindered kinetics caused through cation substitution. However, after 100 (Fig. S16(b), (c), (e) and (f)) and 200 cycles, the charge transfer resistance for the parent LNO increases significantly while that of the 1Mg1W-LNO sample undergoes a much smaller growth. The improved surface impedance characteristics on coat-doping signified decreased surface degradation leading to the increased capacity retention observed consistently across long-term cycling. The cross-sectional SEM images of LNO and 1Mg1W-LNO electrodes harvested from 3E cells after 200 cycles (CC only charging) are shown in Fig. 8(f) and (g), respectively. Significant particle pulverisation is seen across many secondary particles across the LNO electrode, arising from repeated microcracks originating during cycling. In contrast, no significant particle pulverisation is observed across the 1Mg1W-LNO electrode. Microcrack suppression here is likely caused by the smoother phase transition behaviour associated with the doped LNO materials. The altered primary particle morphology also plays a role, where the smaller, more rod-like particles are able to more effectively dissipate internal strains arising from the anisotropic lattice distortions.[55] Relieving particle microcracking and pulverisation through this doping method thus minimises the proliferation of fresh surfaces vulnerable to electrolyte attack and reduces the extent of surface degradation, reflected across the improved cycling stability and impedance results reported here.

Conclusions

In this work a dual cation substituted Mg/W-LiNiO$_2$ cathode was synthesised to evaluate the effectiveness of employing a dual coating-doping strategy in stabilising the electrochemical stability of polycrystalline LiNiO$_2$-based cathode active materials. The success of this was observed with the 1Mg1W-LNO composition delivering improved cycling stabilities compared to unmodified and single-substituted samples, retaining 85% of its specific capacity after 100 cycles in half-cells. However, W-containing LNO cathodes here generally displayed lower specific capacities, attributed to higher off-stoichiometries occurring on W incorporation – up to 4.5 and 6.2% for 1W-

LNO and 2W-LNO, respectively. XRD-CT measurements on *ex situ* cathodes at different states of charge revealed inhomogeneity in the structural transformations for W-containing samples (both single and coat-doped LNO) during delithiation, prompting a review of the synthetic procedure. By increasing the molar excess of the LiOH·H$_2$O precursor used during calcination from 1 to 5%, W-containing LNOs exhibiting greater layered character and reduced off-stoichiometries were produced, leading to higher initial specific capacities, with all displaying enhanced stability compared to undoped LNO. In particular, 1Mg1W-LNO prepared through this adapted route retained 91% of its initial capacity after 100 cycles, showing the highest stability enhancement across the compositional series presented here. Further studies in full-cells confirm the stabilising nature of the coat-doping strategy across higher mass loading electrode specifications and cell formats. The improved stability of this coat-doped LiNiO$_2$ highlights the advantages of targeted compositional tuning of ultra-Ni-rich cathode materials.

Author contributions

BIJJ: conceptualisation, investigation, formal analysis, writing – original draft, writing – review and editing, visualisation. SB: investigation, formal analysis, writing – review and editing, visualisation. SWTP: investigation, software, formal analysis, writing – review and editing, visualisation, funding acquisition. AGS: investigation, software, formal analysis, writing – reviewing and editing, visualisation. LG: investigation. MA: investigation. JAG: investigation. NSK: investigation. IM: project administration. SGB: conceptualisation, project administration, funding acquisition, investigation. AMB: software, resources, funding acquisition. SDMJ: software, resources, funding acquisition. ASM: project administration. DS: resources, supervision, funding acquisition. LFJP: resources, supervision, funding acquisition. SC: conceptualisation, resources, writing – review and editing, supervision, funding acquisition.

Conflicts of interest

There are no conflicts to declare.

Data availability

The data generated and analysed in this work has been included in the article or as part of the supplementary information (SI). Supplementary information: Fig. S1–S16 and Tables S1 and S2 as referenced in the main text. See DOI: **https://doi.org/10.1039/d5ta05316a**.

Acknowledgements

This journal is © The Royal Society of Chemistry 2025

J. Mater. Chem. A, 2025, **13**, 39077–39096 | **39093**

References

1 R. Schmuch, R. Wagner, G. Hörpel, T. Placke and M. Winter, *Nat. Energy*, 2018, **3**, 267–278.

2 Y. Ding, Z. P. Cano, A. Yu, J. Lu and Z. Chen, *Electrochem. Energy Rev.*, 2019, **2**, 1–28.

3 S. G. Booth, A. J. Nedoma, N. N. Anthonisamy, P. J. Baker, R. Boston, H. Bronstein, S. J. Clarke, E. J. Cussen, V. Daramalla, M. De Volder, S. E. Dutton, V. Falkowski, N. A. Fleck, H. S. Geddes, N. Gollapally, A. L. Goodwin, J. M. Griffin, A. R. Haworth, M. A. Hayward, S. Hull, B. J. Inkson, B. J. Johnston, Z. Lu, J. L. MacManus-Driscoll, X. Martínez De Irujo Labalde, I. McClelland, K. McCombie, B. Murdock, D. Nayak, S. Park, G. E. Pérez, C. J. Pickard, L. F. J. Piper, H. Y. Playford, S. Price, D. O. Scanlon, J. C. Stallard, N. Tapia-Ruiz, A. R. West, L. Wheatcroft, M. Wilson, L. Zhang, X. Zhi, B. Zhu and S. A. Cussen, *APL Mater.*, 2021, **9**, 109201.

4 W. Li, E. M. Erickson and A. Manthiram, *Nat. Energy*, 2020, **5**, 26–34.

5 J. Xu, F. Lin, M. M. Doeff and W. Tong, *J. Mater. Chem. A*, 2017, **5**, 874–901.

6 B. K. Sovacool, *Extr. Ind. Soc.*, 2019, **6**, 915–939.

7 J. U. Choi, N. Voronina, Y.-K. Sun and S.-T. Myung, *Adv. Energy Mater.*, 2020, **10**, 2002027.

8 W. Li, S. Lee and A. Manthiram, *Adv. Mater.*, 2020, **32**, 2002718.

9 M. Bianchini, M. Roca-Ayats, P. Hartmann, T. Brezesinski and J. Janek, *Angew. Chem., Int. Ed.*, 2019, **58**, 10434–10458.

10 E. Rossen, C. D. W. Jones and J. R. Dahn, *Solid State Ionics*, 1992, **57**, 311–318.

11 J. Xu, E. Hu, D. Nordlund, A. Mehta, S. N. Ehrlich, X.-Q. Yang and W. Tong, *ACS Appl. Mater. Interfaces*, 2016, **8**, 31677–31683.

12 M. Jiang, D. L. Danilov, R.-A. Eichel and P. H. L. Notten, *Adv. Energy Mater.*, 2021, **11**, 2103005.

13 T. Li, X.-Z. Yuan, L. Zhang, D. Song, K. Shi and C. Bock, *Electrochem. Energy Rev.*, 2020, **3**, 43–80.

14 L. Mu, Z. Yang, L. Tao, C. K. Waters, Z. Xu, L. Li, S. Sainio, Y. Du, H. L. Xin, D. Nordlund and F. Lin, *J. Mater. Chem. A*, 2020, **8**, 17487–17497.

15 Y. You, H. Celio, J. Li, A. Dolocan and A. Manthiram, *Angew. Chem., Int. Ed.*, 2018, **57**, 6480–6485.

16 N. V. Faenza, L. Bruce, Z. W. Lebens-Higgins, I. Plitz, N. Pereira, L. F. J. Piper and G. G. Amatucci, *J. Electrochem. Soc.*, 2017, **164**, A3727.

17 W. M. Seong, Y. Kim and A. Manthiram, *Chem. Mater.*, 2020, **32**, 9479–9489.

18 R. Jung, M. Metzger, F. Maglia, C. Stinner and H. A. Gasteiger, *J. Electrochem. Soc.*, 2017, **164**, A1361.

19 S. Ahmed, M. Bianchini, A. Pokle, M. S. Munde, P. Hartmann, T. Brezesinski, A. Beyer, J. Janek and K. Volz, *Adv. Energy Mater.*, 2020, **10**, 2001026.

20 F. Kong, C. Liang, L. Wang, Y. Zheng, S. Perananthan, R. C. Longo, J. P. Ferraris, M. Kim and K. Cho, *Adv. Energy Mater.*, 2019, **9**, 1802586.

21 W. Li, H. Y. Asl, Q. Xie and A. Manthiram, *J. Am. Chem. Soc.*, 2019, **141**, 5097–5101.

22 W. Li, J. N. Reimers and J. R. Dahn, *Solid State Ionics*, 1993, **67**, 123–130.

23 L. de Biasi, A. Schiele, M. Roca-Ayats, G. Garcia, T. Brezesinski, P. Hartmann and J. Janek, *ChemSusChem*, 2019, **12**, 2240–2250.

24 H. Li, N. Zhang, J. Li and J. R. Dahn, *J. Electrochem. Soc.*, 2018, **165**, A2985.

25 P. H. Chien, X. Wu, B. Song, Z. Yang, C. K. Waters, M. S. Everett, F. Lin, Z. Du and J. Liu, *Batteries Supercaps*, 2021, **4**, 1701–1707.

26 I. McClelland, S. G. Booth, N. N. Anthonisamy, L. A. Middlemiss, G. E. Pérez, E. J. Cussen, P. J. Baker and S. A. Cussen, *Chem. Mater.*, 2023, **35**, 4149–4158.

27 L. Croguennec, C. Pouillerie, A. N. Mansour and C. Delmas, *J. Mater. Chem.*, 2001, **11**, 131–141.

28 C. S. Yoon, D.-W. Jun, S.-T. Myung and Y.-K. Sun, *ACS Energy Lett.*, 2017, **2**, 1150–1155.

29 A. O. Kondrakov, A. Schmidt, J. Xu, H. Geßwein, R. Mönig, P. Hartmann, H. Sommer, T. Brezesinski and J. Janek, *J. Phys. Chem. C*, 2017, **121**, 3286–3294.

30 G. Conforto, R. Ruess, D. Schröder, E. Trevisanello, R. Fantin, F. H. Richter and J. Janek, *J. Electrochem. Soc.*, 2021, **168**, 070546.

31 L. Wheatcroft, A. Bird, J. C. Stallard, R. L. Mitchell, S. G. Booth, A. J. Nedoma, M. F. L. De Volder,

39094 | *J. Mater. Chem. A*, 2025, **13**, 39077–39096

This journal is © The Royal Society of Chemistry 2025

S. A. Cussen, N. A. Fleck and B. J. Inkson, *Batteries Supercaps*, 2023, **6**, e202300032.

32 A. R. Haworth, B. I. J. Johnston, L. Wheatcroft, S. L. McKinney, N. Tapia-Ruiz, S. G. Booth, A. J. Nedoma, S. A. Cussen and J. M. Griffin, *ACS Appl. Mater. Interfaces*, 2024, **16**, 7171–7181.

33 C. Delmas, M. Ménétrier, L. Croguennec, I. Saadoune, A. Rougier, C. Pouillerie, G. Prado, M. Grüne and L. Fournès, *Electrochim. Acta*, 1999, **45**, 243–253.

34 Y. P. Wu, E. Rahm and R. Holze, *Electrochim. Acta*, 2002, **47**, 3491–3507.

35 K. Zhou, Q. Xie, B. Li and A. Manthiram, *Energy Storage Mater.*, 2021, **34**, 229–240.

36 M. Guilmard, L. Croguennec, D. Denux and C. Delmas, *Chem. Mater.*, 2003, **15**, 4476–4483.

37 S. Madhavi, G. V. Subba Rao, B. V. R. Chowdari and S. F. Y. Li, *J. Power Sources*, 2001, **93**, 156–162.

38 D. Weber, J. Lin, A. Pokle, K. Volz, J. Janek, T. Brezesinski and M. Bianchini, *J. Electrochem. Soc.*, 2022, **169**, 030540.

39 F. Du, L. Ding, W. Shi, Y. Wang, Z. Fan, Y. Li and J. Zheng, *Ceram. Int.*, 2023, **49**, 9924–9931.

40 Q. Xie, W. Li and A. Manthiram, *Chem. Mater.*, 2019, **31**, 938–946.

41 S. Deng, Y. Li, Q. Dai, J. Fu, Y. Chen, J. Zheng, T. Lei, J. Guo, J. Gao and W. Li, *Sustainable Energy Fuels*, 2019, **3**, 3234–3243.

42 J. D. Steiner, H. Cheng, J. Walsh, Y. Zhang, B. Zydlewski, L. Mu, Z. Xu, M. M. Rahman, H. Sun, F. M. Michel, C.-J. Sun, D. Nordlund, W. Luo, J.-C. Zheng, H. L. Xin and F. Lin, *ACS Appl. Mater. Interfaces*, 2019, **11**, 37885–37891.

43 D. Liu, S. Liu, C. Zhang, L. You, T. Huang and A. Yu, *ACS Sustain. Chem. Eng.*, 2019, **7**, 10661–10669.

44 D. Kitsche, S. Schweidler, A. Mazilkin, H. Geßwein, F. Fauth, E. Suard, P. Hartmann, T. Brezesinski, J. Janek and M. Bianchini, *Mater. Adv.*, 2020, **1**, 639–647.

45 L. Wu, X. Tang, X. Chen, Z. Rong, W. Dang, Y. Wang, X. Li, L. Huang and Y. Zhang, *J. Power Sources*, 2020, **445**, 227337.

46 Y. S. Kim, J. H. Kim, Y.-K. Sun and C. S. Yoon, *ACS Appl. Mater. Interfaces*, 2022, **14**, 17500–17508.

47 K.-J. Park, H.-G. Jung, L.-Y. Kuo, P. Kaghazchi, C. S. Yoon and Y.-K. Sun, *Adv. Energy Mater.*, 2018, **8**, 1801202.

48 C. Xu, W. Xiang, Z. Wu, L. Qiu, Y. Ming, W. Yang, L. Yue, J. Zhang, B. Zhong, X. Guo, G. Wang and Y. Liu, *Chem. Eng. J.*, 2021, **403**, 126314.

49 Z. Cui, Q. Xie and A. Manthiram, *ACS Appl. Mater. Interfaces*, 2021, **13**, 15324–15332.

50 G.-X. Huang, R.-H. Wang, X.-Y. Lv, J. Su, Y.-F. Long, Z.-Z. Qin and Y.-X. Wen, *J. Electrochem. Soc.*, 2022, **169**, 040533.

51 C. Pouillerie, L. Croguennec, P. Biensan, P. Willmann and C. Delmas, *J. Electrochem. Soc.*, 2000, **147**, 2061.

52 K. Min, S.-W. Seo, Y. Y. Song, H. S. Lee and E. Cho, *Phys. Chem. Chem. Phys.*, 2017, **19**, 1762–1769.

53 G.-T. Park, D. R. Yoon, U.-H. Kim, B. Namkoong, J. Lee, M. M. Wang, A. C. Lee, X. W. Gu, W. C. Chueh, C. S. Yoon and Y.-K. Sun, *Energy Environ. Sci.*, 2021, **14**, 6616–6626.

54 N.-Y. Park, S.-B. Kim, M.-C. Kim, S.-M. Han, D.-H. Kim, M.-S. Kim and Y.-K. Sun, *Adv. Energy Mater.*, 2023, 2301530.

55 H.-H. Ryu, K.-J. Park, D. R. Yoon, A. Aishova, C. S. Yoon and Y.-K. Sun, *Adv. Energy Mater.*, 2019, **9**, 1902698.

56 C. Geng, D. Rathore, D. Heino, N. Zhang, I. Hamam, N. Zaker, G. A. Botton, R. Omessi, N. Phattharasupakun, T. Bond, C. Yang and J. R. Dahn, *Adv. Energy Mater.*, 2022, **12**, 2103067.

57 H.-H. Ryu, G.-T. Park, C. S. Yoon and Y.-K. Sun, *J. Mater. Chem. A*, 2019, **7**, 18580–18588.

58 D. Goonetilleke, A. Mazilkin, D. Weber, Y. Ma, F. Fauth, J. Janek, T. Brezesinski and M. Bianchini, *J. Mater. Chem. A*, 2022, **10**, 7841–7855.

59 L. Mu, W. H. Kan, C. Kuai, Z. Yang, L. Li, C.-J. Sun, S. Sainio, M. Avdeev, D. Nordlund and F. Lin, *ACS Appl. Mater. Interfaces*, 2020, **12**, 12874–12882.

60 L. Mu, R. Zhang, W. H. Kan, Y. Zhang, L. Li, C. Kuai, B. Zydlewski, M. M. Rahman, C.-J. Sun, S. Sainio, M. Avdeev, D. Nordlund, H. L. Xin and F. Lin, *Chem. Mater.*, 2019, **31**, 9769–9776.

61 W. M. Seong and A. Manthiram, *ACS Appl. Mater. Interfaces*, 2020, **12**, 43653–43664.

62 B. H. Toby and R. B. Von Dreele, *J. Appl. Crystallogr.*, 2013, **46**, 544–559.

63 A. S. Menon, N. Shah, J. A. Gott, E. Fiamegkou, M. J. W. Ogley, G. J. Páez Fajardo, N. Vaenas, I. Ellis, N. Ravichandran, P. Cloetens, D. Karpov, J. M. Warnett, P. Malliband, D. Walker, G. West, M. Loveridge and L. F. J. Piper, *PRX Energy*, 2024, **3**, 013004.

64 A. Vamvakeros, A. A. Coelho, D. Matras, H. Dong, Y. Odarchenko, S. W. T. Price, K. T. Butler, O. Gutowski, A.-C. Dippel, M. Zimmermann, I. Martens, J. Drnec, A. M. Beale and S. D. M. Jacques, *J. Appl. Crystallogr.*, 2020, **53**, 1531–1541.

65 A. Vamvakeros, S. D. M. Jacques, M. Di Michiel, P. Senecal, V. Middelkoop, R. J. Cernik and A. M. Beale, *J. Appl. Crystallogr.*, 2016, **49**, 485–496.

66 G. Ashiotis, A. Deschildre, Z. Nawaz, J. P. Wright, D. Karkoulis, F. E. Picca and J. Kieffer, *J. Appl. Crystallogr.*, 2015, **48**, 510–519.

67 A. Vamvakeros, S. D. M. Jacques, M. Di Michiel, V. Middelkoop, C. K. Egan, R. J. Cernik and A. M. Beale, *J. Appl. Crystallogr.*, 2015, **48**, 1943–1955.

68 H. Dong, S. D. M. Jacques, E. Papoutsellis, A. M. Beale and A. Vamvakeros, *ChemRxiv*, 2025, preprint, DOI: **10.26434/chemrxiv-2025-m1v5v**.

69 C. Jacquot, A. Vamvakeros, A. Pavlišič, S. W. T. Price, H. Dong, D. Matras, L. Protasova, B. Likozar, S. D. M. Jacques, A. M. Beale and V. Middelkoop, *Chem. Eng. J. Adv.*, 2023, **16**, 100538.

70 G. Kresse and J. Hafner, *Phys. Rev. B: Condens. Matter Mater. Phys.*, 1993, **47**, 558–561.

71 G. Kresse and J. Hafner, *Phys. Rev. B: Condens. Matter Mater. Phys.*, 1993, **48**, 13115–13118.

72 G. Kresse and J. Furthmüller, *Phys. Rev. B: Condens. Matter Mater. Phys.*, 1996, **54**, 11169–11186.

This journal is © The Royal Society of Chemistry 2025

J. Mater. Chem. A, 2025, **13**, 39077–39096 | **39095**

73 G. Kresse and J. Furthmüller, *Comput. Mater. Sci.*, 1996, **6**, 15–50.

74 A. G. Squires, L. Ganeshkumar, C. N. Savory, S. R. Kavanagh and D. O. Scanlon, *ACS Energy Lett.*, 2024, **9**, 4180–4187.

75 J. Heyd, G. E. Scuseria and M. Ernzerhof, *J. Chem. Phys.*, 2003, **118**, 8207–8215.

76 A. V. Krukau, O. A. Vydrov, A. F. Izmaylov and G. E. Scuseria, *J. Chem. Phys.*, 2006, **125**, 224106.

77 I. Mosquera-Lois, S. R. Kavanagh, A. Walsh and D. O. Scanlon, *npj Comput. Mater.*, 2023, **9**, 25.

78 I. Mosquera-Lois, S. R. Kavanagh, A. Walsh and D. O. Scanlon, *J. Open Source Softw.*, 2022, **7**, 4817.

79 S. R. Kavanagh, A. G. Squires, A. Nicolson, I. Mosquera-Lois, A. M. Ganose, B. Zhu, K. Brlec, A. Walsh and D. O. Scanlon, *J. Open Source Softw.*, 2024, **9**, 6433.

80 C. Freysoldt, J. Neugebauer and C. G. Van de Walle, *Phys. Rev. Lett.*, 2009, **102**, 016402.

81 J. Buckeridge, D. O. Scanlon, A. Walsh and C. R. A. Catlow, *Comput. Phys. Commun.*, 2014, **185**, 330–338.

82 A. G. Squires, D. O. Scanlon and B. J. Morgan, *J. Open Source Softw.*, 2023, **8**, 4962.

83 J. Buckeridge, *Comput. Phys. Commun.*, 2019, **244**, 329–342.

84 A. van Bommel and J. R. Dahn, *J. Electrochem. Soc.*, 2009, **156**, A362.

85 X. Li, L. Zhou, H. Wang, D. Meng, G. Qian, Y. Wang, Y. He, Y. Wu, Z. Hong, Z.-F. Ma and L. Li, *J. Mater. Chem. A*, 2021, **9**, 19675–19680.

86 H.-H. Ryu, N.-Y. Park, D. R. Yoon, U.-H. Kim, C. S. Yoon and Y.-K. Sun, *Adv. Energy Mater.*, 2020, **10**, 2000495.

87 L. Wang, B. Zhu, D. Xiao, X. Zhang, B. Wang, H. Li, T. Wu, S. Liu and H. Yu, *Adv. Funct. Mater.*, 2023, **33**, 2212849.

88 U. H. Kim, D. W. Jun, K. J. Park, Q. Zhang, P. Kaghazchi, D. Aurbach, D. T. Major, G. Goobes, M. Dixit, N. Leifer, C. M. Wang, P. Yan, D. Ahn, K. H. Kim, C. S. Yoon and Y. K. Sun, *Energy Environ. Sci.*, 2018, **11**, 1271–1279.

89 C. Pouillerie, E. Suard and C. Delmas, *J. Solid State Chem.*, 2001, **158**, 187–197.

90 D. Weber, J. Lin, A. Pokle, K. Volz, J. Janek, T. Brezesinski and M. Bianchini, *J. Electrochem. Soc.*, 2022, **169**, 030540.

91 Y. Koyama, H. Arai, I. Tanaka, Y. Uchimoto and Z. Ogumi, *Chem. Mater.*, 2012, **24**, 3886–3894.

92 N. Phattharasupakun, M. M. E. Cormier, E. Lyle, E. Zsoldos, A. Liu, C. Geng, Y. Liu, H. Li, M. Sawangphruk and J. R. Dahn, *J. Electrochem. Soc.*, 2021, **168**, 090535.

93 C. Delmas, J. P. Pérès, A. Rougier, A. Demourgues, F. Weill, A. Chadwick, M. Broussely, F. Perton, P. Biensan and P. Willmann, *J. Power Sources*, 1997, **68**, 120–125.

94 S. Sicolo, M. Sadowski, K. Vettori, M. Bianchini, J. Janek and K. Albe, *Chem. Mater.*, 2024, **36**, 492–500.

95 Z. Guo, Z. Cui and A. Manthiram, *ACS Energy Lett.*, 2024, 3316–3323, DOI: **10.1021/acsenergylett.4c01027**.

96 J.-H. Kim, H.-H. Ryu, S. J. Kim, C. S. Yoon and Y.-K. Sun, *ACS Appl. Mater. Interfaces*, 2019, **11**, 30936–30942.

97 M. E. Arroyo y de Dompablo and G. Ceder, *Chem. Mater.*, 2003, **15**, 63–67.

98 W. Hua, J. Chen, D. Ferreira Sanchez, B. Schwarz, Y. Yang, A. Senyshyn, Z. Wu, C.-H. Shen, M. Knapp, H. Ehrenberg, S. Indris, X. Guo and X. Ouyang, *Angew. Chem., Int. Ed.*, 2024, **63**, e202403189.

99 A. M. Boyce, E. Martínez-Pañeda, A. Wade, Y. S. Zhang, J. J. Bailey, T. M. M. Heenan, D. J. L. Brett and P. R. Shearing, *J. Power Sources*, 2022, **526**, 231119.

100 T. Zhao, J. Zhang, K. Wang, Y. Xiao, Q. Wang, L. Li, J. Tseng, M.-C. Chen, J.-J. Ma, Y.-R. Lu, I. Hirofumi, Y.-C. Shao, X. Zhao, S.-F. Hung, Y. Su, X. Mu and W. Hua, *Angew. Chem., Int. Ed.*, 2025, **64**, e202419664.

39096 | *J. Mater. Chem. A*, 2025, **13**, 39077–39096

This journal is © The Royal Society of Chemistry 2025